Collapsing solutions to the 3-D Euler equations

Alain Pumir
Ecole Normale Supérieure, Département de Physique, 24 rue Lhomond, 75231 Paris Cedex 05, France and C. E. N. Saclay, 91191 Gif-s/Yvette, France

Eric Siggia
Ecole Normale Supérieure, Département de Physique, 24 rue Lhomond, 75231 Paris Cedex 05, France and Laboratory of Atomic and Solid State Physics, Cornell University, Ithaca, New York 14853-2501

(Received 30 June 1989; accepted 18 October 1989)

A three-dimensional adaptive mesh code is used to search for singularities in the incompressible Euler equations. For the initial conditions examined, the maximum vorticity eventually grows only exponentially. The small scales are quasi-two-dimensional and the vorticity has a pronounced tendency to develop sharp jumps in magnitude. The vorticity is very nearly parallel to the eigenvector of the rate-of-strain matrix whose eigenvalue is the smallest in magnitude. This eigenvalue is positive and much smaller than the others.

I. INTRODUCTION

The computational experiments reported in this paper examine a problem that has three distinct aspects: physical, mathematical, and numerical. Physically, they touch on our earlier speculations[1,2] as to the root causes of boundary layer intermittency, which is a well-established phenomenon experimentally[3,4] but for which a convincing theory is lacking. The mathematical aspects enter since we suppose that understanding how singularities could develop in the Euler equations is equivalent to asking how vorticity and strain can be most effectively coupled to transfer energy to small scales. Turbulent boundary layers do this efficiently and in a very time-dependent manner. Finally, the technical aspects of this study evolve around ways to quantitatively simulate the fluid equations over a range of scales far greater than is possible with a conventional code. To even hope to do this requires compromises; our methods only apply to the singularity problem, but, otherwise, there is no hope of reaching asymptotic scales. We elaborate on these three points in turn.

Turbulent boundary layers appear simple at the level of one-point statistics such as the mean velocity and Reynolds stress as a function of distance from the wall.[5] The von Kármán theory and its elaborations are quite satisfactory.[5–7] But the time recordings that yield these regular averages are highly irregular. Very small scales are excited, in fact, too small to be fully resolved with hot wires.[8] Higher derivative statistics and higher moments of the first derivative are non-Gaussian[9] and much larger than one would estimate from an average viscous cutoff. Extensive conditional sampling has shown that these fluctuations occur as organized bursts extending from several viscous lengths from the wall to beyond the von Kármán region.[10,11] By a suitable choice of threshold, bursts can be defined so that they occur less than 10% of the time yet contribute more than half of the Reynolds stress.[11,12]

Flow visualization experiments have provided an essential qualitative understanding of the origin of these bursts, by linking them to a vortical structure in the shape of a hairpin.[4,13] The pictures, probably due to inherent limitations in the technique, are less dramatic at high Reynolds numbers than for low ones and provide no insight into the dynamics of the small scales responsible for the large derivative statistics. We also have found no definitive experimental answer to whether all the vorticity production can be attributed to passive stretching by the mean flow or whether something more local and nonlinear is required to explain observations. Also, nothing is known about the local vorticity–strain correlation. Numerical simulation is thus a useful bridge between experiment and linearized theories.[14,15]

Rigorous, controlled theory has not gone beyond the stage of a "universal" secondary instability that is rapidly growing and three dimensional.[16] The physics involved, namely an uplifting and rotation of vorticity out of the spanwise direction, is not at variance with the idea of a hairpin. Simulations of turbulent channel flow support this association.[14,15]

One might hope that some equally universal mechanistic explanation can be given for the smallest scales of motion. Intermittency often has been attributed to vortex tubes and sheets since its discovery.[17,18] Always lacking was a means for stabilizing these structures. We therefore propose the next simplest alternative, namely, that the "structure" should be sought in space-time as a collapse. The boundary layer is a particularly appealing case to study since the flow configuration that seemed most likely on theoretical grounds to yield a singularity resembled a hairpin vortex.[1]

Hunting for singularities in the Euler equations is by now a developed sport. Two general approaches have been followed, loosely speaking, Fourier modes[19] and vorticity dynamics,[20,21] which clearly must agree if done quantitatively but imply a differing intuition about what causes the singularity. The Fourier calculations imagine that beating modes together by a nonlinear term will lead to a finite time singularity, (e.g., infinite ω or enstrophy). The flow in real space is irrelevant and could be fractal in some sense.[22] Vorticity dynamics operates in real space and tries to arrange for the flow to generate a strain rate that diverges with the maximum vorticity and is oriented so as to make the vorticity blow up in a finite time. From this vantage point it is not evident why a fractal vorticity distribution is an advantage,

 0899-8213/90/020220-22$02.00

since the folds will tend to cancel out of the integral that relates strain to vorticity. The simplest possibility would be just a self-similar pointwise collapse and its elaborations.[7]

The technical requirements of our program require a real space-vorticity approach since to simulate a large range of scales we are constrained to use the same number of modes independent of scale size, redistributed, of course, to resolve the smallest scales. The algorithm is straightforward when the solution is reasonably compact or confined and a number of one-dimensional problems (either one linear or a radial direction) have been treated with great accuracy in this way.[23,24] In two dimensions there exist sophisticated multigrid algorithms that are capable of adaptively putting down coordinate patches of varying resolution where needed to resolve the flow.[25]

To build such an elaborate code in three dimensions was beyond our capabilities and perhaps unwarranted in view of the absence of any real understanding of how the singularities look. Instead we used separable coordinates in three dimensions; unfortunately the collapse was probably not self-similar nor very compact. Ultimately our algorithm broke down, but only after we reached scales far smaller than any plausible viscous cutoff and a factor of nearly 100 smaller than a fixed mesh code could do with comparable resolution on the large scales initially and on the small scales finally.[26] We were also able to understand the fluid dynamical processes that led to the dispersal of the vorticity and develop some intuition as to the probable asymptotic dynamics. We did not find a singularity for any of the initial conditions examined.

We organize our presentation as follows. Section II contains a summary of mathematical results that place constraints on singularities if they exist. We discuss our numerical algorithm in Sec. III and give an order of magnitude estimate of all sources of errors. A more precise statement of errors for the principal run at specific times is left for the Appendix.

The initial conditions that we ran furthest in time were a pair of antiparallel vortex tubes. This was suggested by an earlier study of vortex filaments interacting through the Biot–Savart law, which gave a singularity for reasons that could be readily understood.[1] A number of simulations with fixed meshes followed that showed considerable core deformation but were unclear as to what happened asymptotically and why.[27–31] In Sec. IV we demonstrate that the initial distortion of the core can be understood from the Biot–Savart model and then follow the distortion down to very small scales. No singularity is found, but instead the flow evolves toward a two-dimensional form and the strain component parallel to the vorticity ceases to grow.

In Sec. V we look at other initial conditions with both higher and lower symmetry in an effort to keep the large component of the strain parallel to the vorticity. In various ways the strain always manages to become passive. Purely for its relevance to the dynamics of the tip of a hairpin, we include a simulation of a parabolic vortex tube and show how the core distorts around the point of greatest curvature.

In the conclusion, Sec. VI, we discuss parallels between our simulations and others which concentrate on small scales. Similarities in vorticity–strain correlations are apparent, which for our geometries are accompanied by "vortex steps." We attempt to quantify and explain in what sense the flow becomes locally two dimensional on small scales. Finally, we emphasize the possibly nongeneric features of our initial conditions and speculate on what type of singularities could have escaped detection.

II. MATHEMATICAL PRELIMINARIES

Rigorous analysis has provided several important constraints on the nature of singularities in the three-dimensional Navier–Stokes and Euler equations without either disproving or proving their existence. What is known, provides essential guidance to any numerical study, so we briefly summarize what we need. The question posed can be simply stated: Assume that the initial conditions are infinitely differentiable in space, how do they loose smoothness as a function of time?

For the Euler equations it has been shown[32] that the growth of the L^2 norm of any velocity derivative is bounded by the supremum over space of the vorticity, $\sup|\omega|$, specifically

$$\int(\partial^k v)^2(t) \leq \int(\partial^k v)^2(0) \times \exp\left(\text{cst}\int_0^t \sup|\omega|(t')dt'\right), \tag{1}$$

where cst is a fixed constant. It is therefore possible for a singularity to occur with the enstrophy finite. Such a singularity might be of limited physical interest since it would not entail the transfer of much energy to small scales; nevertheless, it would stop any numerical integration unless some regularization was employed. To conceive of numerically simulating an Euler singularity, however, requires a stronger result such as would be obtained by replacing the L^2 norm in (1) by $\sup|\partial^k v|$. If a high derivative could become infinite before the lower ones, then it would be invisible to most numerical schemes. Simply counting gradients suggests that if $\sup|\omega|$ is replaced by $\sup|\partial v|$, then the desired result is obtained. It is then quite practical to ensure that the first derivatives are always well resolved. In fact, we always find the antisymmetric piece of $\partial_i v_j$ to be at least as large and to vary at least as rapidly as the symmetric part. Thus controlling $\omega(x,t)$ is sufficient to ensure numerical accuracy.

Results for the Navier–Stokes equations are also phrased indirectly, namely, if a singularity exists then consequences are derived. The most interesting of these, for our purposes, is that of Leray,[33] namely if there is singularity of t^* then

$$\sup|v| \geq \text{cst}[\nu/(t^*-t)]^{1/2}, \tag{2}$$

where ν is the viscosity. Again we find that the singularity cannot hide in high derivatives.[34] For the vorticity, omitting some technicalities, the analog of (2) is[35]

$$\sup|\omega| \geq \text{cst}/(t^*-t).$$

A stronger singularity must occur, if any does, when viscosity is present since the velocity itself must diverge.

The third direction in which one might hope for guid-

ance are comparison theorems between Navier–Stokes and Euler solutions. The one that we are aware of states that if in three-space with no boundaries the Euler solutions have not yet developed singularities, then a sufficiently small viscosity ν will make an $O(\nu)$ change in the solution.[36]

We will assume in the following for the Euler equations that unless the velocity shows signs of diverging as $1/\sqrt{t^* - t}$, the addition of viscosity will cut off the singularity provided the topology of the flow does not change. First, it may be objected that (2) is irrelevant for the Euler equations since there is no viscosity to set the dimensions. But circulation has the same units as viscosity and in a model we studied earlier,[1] it serves to dimensionalize a formula analogous to (2). Further dimensional estimates for that model indeed suggest a singularity for Navier–Stokes is possible since the straining is just large enough to balance viscous diffusion. The caveat about changes in topology is necessary since viscosity breaks the circulation invariants and can qualitatively alter the flow. There are well-known examples where viscosity plus rigid boundaries completely change the linear stability properties of a flow.[6,16] We are unaware of any such examples for free flows. Changes in topology, however, can cause surprises. For instance, in Sec. IV we suggest how viscosity can alter the growth of $\sup|\omega|$ from e^t for Euler to $\exp(e^t)$ by this mechanism. Thus the assumption with which we begin this paragraph is merely an abstraction from several examples.

III. NUMERICAL METHODS

A. Algorithm

In contrast to a standard large eddy simulation, a technically viable code designed to study singularities unavoidably reflects the authors' assumptions about the dynamical processes leading to these singularities. We begin by making these explicit and physically plausible.

Singularities, as argued in Sec. II, involve infinite gradients and arbitrarily small scales. The overriding concern of this study will be to examine as large a range of scales as possible in an effort to reach some asymptotic limit if one exists. A code employing a fixed basis or grid is hopeless for this task. The most efficient of these, a spectral code, cannot handle significantly more than 256^3 modes. At least eight grid points are needed to quantitatively resolve the smallest scales (our finite difference code uses upward of 16), while a factor of 2 to 4 in scale size is needed to insulate the large scales from the periodic boundary conditions. Adequate resolution is essential since the small scales must be allowed to interact among themselves without aliasing. Furthermore, these small scales may carry negligible energy and enstrophy since infinite vorticity can occur with the enstrophy finite. A reasonable energy spectrum is not an adequate measure of resolution for these problems. Under our criterion, a spectral simulation can access less than a factor of 10 in scale size[37] while we have simulated nearly a factor of 10^3.

Clearly some way is needed of readapting the computational modes to the solution as it evolves. Hopefully, the number of relevant modes does not increase significantly in time, which would be true if the dynamics are sufficiently local or the large (nonlocal) scales can be simply parametrized. A self-similar solution with the characteristic spatial scale as a function of time is the simplest case of what we have in mind.

The Euler equations in vorticity form are spatially nonlocal in that the strain depends on a weighted integral of the vorticity. The important component of strain is that along the vorticity which therefore diverges as the logarithmic derivative of the maximum vorticity. Our algorithm presumes that in some sense this singular strain is determined by the same region and range of scales that define the singular vorticity. The problem becomes hopeless if the fine-scale folding of the vorticity in a region well removed from the one under consideration changes the local strain rate. These assumptions can clearly be checked internally as the singularity develops, both numerically by zeroing certain modes and also by a multipole expansion of the strain. They are most plausible when a strong, i.e., power law singularity, is observed.

The tasks of adapting the mesh and controlling the errors were responsible for most of the time expended in developing and utilizing our code. Otherwise, consideration of singularities allows several simplifications. Boundary conditions and the specifics of large scales should be unimportant asymptotically if a singularity exists. (They add a constant strain to a diverging one.) Also, since we are always resolving well the smallest scales on a greatly stretched time axis, the flow looks laminar. This is virtually a tautology, but means that it is trivial and unambiguous to assess what constitutes adequate resolution. Any study that purports to solve the Euler equations quantitatively near the first singularity cannot afford to employ less resolution than we do.

In this paper we will be almost exclusively concerned with the Euler equations so the question of numerical versus physical instabilities may seem acute. Actually this problem is more ostensible than real. By linearizing we know that the smallest scales are the most prone to numerical instabilities that are easy to detect by Fourier spectra on the logical mesh or graphically. When weight on small scales (a few mesh spacings) is negligible and not increasing, we assume that the large scales are evolving physically. An example is given at the end of this section to illustrate the appearance of numerical noise. In a sense we are always resolving the fastest growing physical instability. This self-stretching, which is a feature of all our solutions, helps to suppress unwanted numerical effects.

Another notion of stability should also be mentioned here, namely, does the singularity attract all solutions in its neighborhood (a stable instability)? Is the asymptotic solution, to within scale factors, the same for an open set of initial conditions? The methods employed in this paper permit us to detect only attracting singularities. We return to this question in Sec. VI.

To allow for spatially varying resolution as simply as possible and facilitate its subsequent readjustments, we chose to use finite differences on separable rectangular coordinates. More elaborate schemes that put local coordinate patches where needed have been implemented in lower dimensions[23–25] but are not essential for our initial conditions for the times over which they have been followed. Vortex

methods are also well suited to adaptive algorithms but appear to be rather noisy and expensive in three dimensions when some accuracy is desired.[20,21]

On the scale set by the singularity, the boundaries tend to infinity. We therefore recognize this fact immediately and map the real line denoted by x onto the interval $\xi\epsilon[-1,1]$. A uniform grid is layed down in ξ and all quantities vanish at $\xi = \pm 1$. The following function proved adequate for our purposes:

$$X = \{\alpha - \beta \sin[(\pi/2)\xi] - \gamma \cos(\pi\xi)\} \times \tan[(\pi/2)\xi], \tag{3}$$

where α, β, and γ are constants chosen to keep $dx/d\xi > 0$. One then finds

$$\begin{aligned} &x(\xi \sim 0) = (\pi/2)(\alpha - \gamma)\xi, \\ &x(\xi \gtrsim -1) = (2/\pi)(\alpha + \beta + \gamma)/(\xi + 1), \\ &x(\xi \lesssim 1) = (2/\pi)(\alpha - \beta + \gamma)/(1 - \xi). \end{aligned} \tag{4}$$

Equation (3) increases the spacing between mesh points as x^2 near infinity which smoothly terminates the solution without "wasting" too many points. A more rapid dilation of the mesh near infinity would lead to increased errors in the velocity and its integrals (the velocity varies as x^{-1} or x^{-2} depending on direction and distance). The constants in (4) define the "inner" and "outer" length scales.

The Euler equations were time stepped for the velocity and the nonlinear term was written as velocity cross vorticity. All derivatives were approximated as

$$\frac{d\phi}{dx}(\xi_i) = \left(\frac{dx}{d\xi_i}\right)^{-1} \frac{[\phi(\xi_{i+1}) - \phi(\xi_{i-1})]}{(2\Delta\xi)} + O(\Delta\xi)^2, \tag{5}$$

where a single dummy function ϕ is used irrespective of argument. In order for the finite difference equations to conserve energy and momentum it is necessary to define the integral,

$$\int_{-\infty}^{\infty} \phi\, dx = \Delta\xi \sum_i \left(\frac{dx}{d\xi_i}\right)\phi(\xi_i). \tag{6}$$

To ensure that $v \wedge \omega - \nabla p$ is incompressible on the lattice, the Laplace operator for the pressure has to be defined as two centered differences, Eq. (5), and therefore couples the points $i-2, i, i+2$. The pressure equation therefore decouples on the odd and even sublattices, and the number of mesh points (including $\pm\infty$), must be even. If we number points from 1, ($\xi = -1$) to $2n$ ($\xi = +1$), then the boundary conditions on the even mesh read (with $dx/d\xi$ factors suppressed),

$$\begin{aligned} &(\nabla^2 p)_2 = p_4 - p_2, \\ &(\nabla^2 p)_{2n-2} = -2p_{2n-2} + p_{2n-4}. \end{aligned} \tag{7}$$

The first line of (7) follows by defining a fictitious point 0, writing the usual three-point formula for the second derivative, and then insisting that the pressure has zero derivative at infinity, viz.,

$$0 = \frac{dp}{dx}(\xi = -1) = (p_2 - p_0),$$

whereas in the second line we have simply used $p_{2n} = 0$. On the odd mesh we use boundary conditions $p = 0$ at $-\infty$ and $\partial p/\partial x = 0$ at $+\infty$.[38]

It may now be verified that the finite difference expression for ∇p integrates to zero on the lattice and so energy is conserved. To demonstrate momentum conservation, the pressure trivially disappears but some care is needed to rearrange $v \wedge \omega$. For the special case of a vortex ring, the velocity decreases as r^{-3} for large r and so the momentum integral is ill-defined and the finite difference form will not appear conserved unless suitable symmetry planes are present.

Since upward of 90% of the computational effort went into solving the pressure equation it is important that symmetries be easy to exploit. When reflection planes coincide with $x = 0$ it suffices to find p on the even sublattice only since the symmetry will fill in the odd sublattice. The Poisson inversion was done with the algorithm of Ref. 39 and involved order log (N) operations per point.

The time stepping was by leapfrog with an occasional second-order Runge–Kutta step to initialize and mix the even and odd times. If applied to the one-dimensional advection equation, the leapfrog is neutrally stable while the Runge–Kutta is unstable in fourth order, i.e., $[(\Delta tv/\Delta x)\sin(k)]^4$, where k is the wave vector of the perturbation. We do not believe that this one-dimensional model is a realistic representation of our equations, though clearly we always have to respect a Courant condition.

Numerical errors are most likely to occur for large k and can be easily monitored by taking a Fourier transform with respect to ξ every time statistics are extracted. The boundary conditions are not a problem since all fields vanish smoothly at $\xi = \pm 1$. When the largest gradients were in the x-y plane, we required the total spectral weight of $\langle(\partial v/\partial x)^2\rangle$ and $\langle(\partial v/\partial y)^2\rangle$ in the last few bands to be of the order of a few percent, and not significantly increasing with time. The accuracy with which the conservation laws are obeyed between remesh operations (which typically involved 100–150 time steps) is also a check on instabilities. For the data of Sec. IV, the energy was conserved to relative order 10^{-5}, the momentum to $O(10^{-3})$, and the circulation in a symmetry plane [actually just $\int_{\infty}^{-\infty} v_y(0,y,0)dy$], to order 10^{-4}. [The Poisson equation was not converged to machine accuracy to save computer time, $\max(\nabla\cdot v)/\max(\omega) \lesssim 10^{-5}$.]

It will be apparent in the runs to follow that solutions which are self-stretching are immune to small scale numerical instabilities. This is not implausible since a dilatation will change the effective wavenumber of any numerical instability and also mix the sublattices. This stretching, even if only passive, is a characteristic feature of our problem and there is no reason not to anticipate and exploit it in the numerical algorithm. We never observed any mesh scale instabilities while time stepping the initial conditions in Secs. IV and V as long as adequate spatial resolution was maintained.

The one stability problem we did encounter seemed associated with repeated remeshes and could easily be controlled through the Poisson operator as we now describe. For obvious reasons (elaborated in Sec. III B), to change meshes we interpolated the vorticity and then found the velocity by solving

$$[\nabla^2]_f v = -\nabla \wedge \omega, \tag{8}$$

where $[\ ]_f$ denotes the Laplacian written on the "fine" mesh, i.e., using points $i-1,i,i+1$. The right-hand side of (8) (and ω) are calculated as a centered difference, Eq. (5), so (8) would not be a tautology even if the grids did not change. We adopted this representation of ∇^2 for the remesh only, in order to mix the odd and even sublattices and eliminate the instability just noted.

This should also suppress any other sublattice oscillations that may have developed during the integration. Quantitative measures of the dissipation thereby introduced, which is minimal, is discussed in Sec. III B.

Occasionally we wanted to treat a physical viscosity which we then included explicitly in the time stepping. The actual values of viscosity we employed were never large enough for this to be a significant source of instability, and the step size was always limited by the Courant condition.

One additional detail will complete the specification of our algorithm. It is clearly inefficient to adjust the coordinates if the solution merely translates without changing in shape. We therefore added a time-dependent, spatially uniform velocity to the code v_∞ so as to keep some predetermined point (e.g., a vorticity weighted center of interest) at the origin. We devised an equation for v_∞ that has $v_\infty = \text{const}$ as a homogeneous solution, could be time-stepped explicitly, and had a source term proportional to the distance that was to be zeroed.

We tested our code on a constant shape but propagating solution ("Batchelor dipole," Ref. 40) to the Euler equations in two dimensions (Fig. 1). The resolution is half what we average in our three-dimensional runs (8 points from symmetry plane to maximum vorticity versus 16) and the noise at the last time is greater than anything to be seen in what follows. Nevertheless, the conservation laws are accurately obeyed (see the caption, Fig. 1) and even though there is no stretching or remeshes to stabilize the integration, the noise grows very slowly; the dipole is kept stationary at the origin by v_∞. With resolution 50% higher, the noise would be barely discernible in the figure.

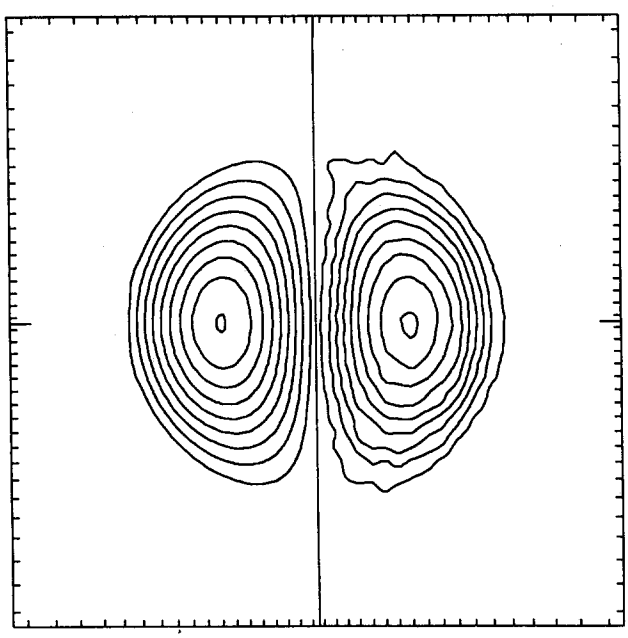

FIG. 1. The Batchelor dipole at $T=0$ (left) and $T=4.5$ (right) showing the appearance of numerical instability for the 2-D Euler equations. Only half the dipole is shown at each time and the interior solid line is the symmetry plane. The maximum velocity of 2.3 and the total length of the horizontal side 2.5 set the scales. The energy, momentum, and circulation are at $T=0$: 8.763 216, 0.937, and 3.57, and at $T=4.5$, 8.763 218, 0.939, and 3.59. The enstrophy changes from 19.92 to 19.95. The noise in the last few spectral bands for $\langle(\partial_x v)^2\rangle$ as defined in the text is 5%.

B. Remesh

This section contains the definition and motivation of how we adjust coordinates. We enumerate the statistics used to control errors and an indication of their general values in sufficient detail to convince the reader that the flow is being quantitatively simulated. A more specific tabulation of errors at several key times is left for the Appendix.

When a singularity assumes a self-similar form with characteristic length and time scales definable by various norms, it is most natural to adjust scales continuously to keep the relevant norms equal to one. For Euler this would mean simulating a scaled velocity V defined as

$$v(x,t) = a(t)V[X = b(t)x, T(t)],$$

for which the scaled equations read (overdot $\equiv d/dt$)

$$\partial_T V = -\frac{\dot{a}}{a\dot{T}}V - \frac{\dot{b}}{b\dot{T}}X\cdot\nabla_X V + \frac{ab}{\dot{T}}(V\cdot\nabla_X V - \nabla_X P), \tag{9}$$

where $\dot{T}$ should be defined as ab.

Several problems arose when we implemented and ran this scheme. Our solution scaled very differently in the x, y, and z directions and in addition both the inner and outer scales [cf. Eq. (4)] had to be separately adjusted. The new linear terms in (9) destroy the explicit conservation of $\int V^2$, and multiplying by X near infinity might cause numerical problems. Also, since the enstrophy and other norms could remain finite while the vorticity diverges[32] it could be dangerous to use them to fix scales.

Since nothing was known about how the singularity would develop, better numerical control could be obtained at the expense of considerable tedium by remeshing at discrete times before the resolution became inadequate. In practice, we examined contour plots of the vorticity vector and demanded that it vary slowly on the mesh in all directions, particularly around the maximum. For the paired vortex solution of Sec. IV this meant that we maintained 12–20 grid points between the symmetry plane and the point of maximum vorticity. In addition, contour plots on the numerical mesh, i.e., as a function of ξ, made it very simple to see how the solution was spread over the mesh (cf. the Appendix). Numerical instabilities could be sensitively monitored by taking a Fourier transform with respect to ξ, as noted above.

We were generally able to keep the total number of mesh points fixed and merely redistribute them in order to maintain resolution. The separability facilitated the interpolation, which was done on the vorticity rather than the velocity. The former is concentrated around the origin where the resolu-

tion is best and is related to the other field by an integral rather than a derivative as would be the case if the velocity were interpolated. Cubic splines were used for the interpolation and a tension parameter was tried but not necessary.

Two additional operations were applied at each remesh near the end of the run in Sec. IV to maintain numerical control, a "cutoff" and a "smoothing." Both might have been avoided at some computational cost and nonseparable coordinates, but the methods we adopted, while clumsy, are controlled and errors can be estimated *a priori*, which we do after presenting the algorithm.

The cutoff consisted of multiplying the vorticity by a function, $1-\exp(-|\xi\pm 1|)/(|\xi_m\pm 1|-|\xi\pm 1|)$ for $|\xi\pm 1|\leqslant|\xi_m\pm 1|$ and one otherwise, so as to reduce it smoothly to zero at infinity and at the same time match smoothly onto 1 for all points closer to the origin than ξ_m that are not affected by the cutoff. If this were not done, vorticity would be pushed to within a few mesh points of infinity by the repeated scale amplifications and the Laplace equation would become impossible to invert accurately.

The "smoothing" was an artificial viscosity applied only to the vorticity well away from the maximum that formed a thin sheet and was advected into a poorly resolved region of space. Obvious instabilities developed when the sheet began to roll up. The diffusion thickened the sheet but maintained the net circulation.

Since the remesh is done at discrete times it is rather simple to assess errors by comparing statistics before and after. Interpolation errors and the sublattice averaging introduced by solving (8) could be evaluated by taking the new velocity and vorticity on the new mesh and interpolating back to the old mesh. Interpolation errors alone were small under all circumstances, and for the vorticity amounted to 0.1% in the vicinity of its maximum. This constituted a supplementary check that the resolution remained adequate. A poorly resolved function is impossible to interpolate accurately. The errors in the velocity in the absence of a cutoff were slightly larger ~0.1%–0.3% since the comparison was made after interpolation and inversion of the "fine mesh" Laplacian in (8) that acted as a numerical viscosity. In addition, we recomputed all derivative statistics from the new velocity to understand how significant the diffusive effects of (8) are by this measure. The maximum over all lattice points of the vorticity invariably decreased by 1%–2% and the maximum mean square strain rate $\mathrm{tr}_{ij}(e_{ij})^2=\frac{1}{4}\mathrm{tr}_{ij}(\partial_i v_j+\partial_j v_i)^2$ by 2%–3%. These relative errors again really just reflect the resolution in that they indicate that the ratio of the Laplacian computed from points $(i\pm 2,i)$ to its value using points $(i\pm 1,i)$ is just 0.98–0.99. Errors in the vorticity–strain correlations were in line with the above. Still with no cutoff, integrals such as energy and enstrophy could change as little as a fraction of a percent up to 5%–10% for the energy depending on how compact the vortical structure is. We infer that the errors are mostly attributable to the discrete approximation (6) for the integral and the slow decrease in the velocity as r tends to infinity.

Particular attention must be paid to errors when the cutoff and smoothing operations are applied at the end of the run with two filaments (Sec. IV). We begin with derivative statistics. The errors in the maximum vorticity and strain were no larger than just noted and therefore entirely attributable to (8). A particularly useful statistic is the local enstrophy production, $\omega\cdot e\cdot\omega$. Its maximum decreased by up to 4%–5%, which is in line with the errors in the individual fields. In the Appendix we also display a contour plot of $\omega\cdot e\cdot\omega/\omega^2$ before and after the remesh and cutoff. In what we consider to be the region of space important for the subsequent evolution, the errors are uniformly small. Finally, to verify that more distant regions do not contaminate the incipient singularity, we repeated a portion of our run with and without a cutoff. The vorticity contour plots at the end are indistinguishable except in the region directly affected by the cutoff.

The cutoff, however, did remove a substantial amount of vorticity and energy due precisely to the large scales of motion that do not participate in the singularity (i.e., contribute negligible strain rate), but which do contribute a mean velocity of translation. Symmetries minimized the influence of large scales since the vorticity removed always had dipolar symmetry. With a cutoff the maximum velocity typically decreased by 10%, the enstrophy by 25%, and the energy by a factor of 2. The substantial decrease in energy is physically interesting, and discussed in Sec. IV, since it implies that the singular region contains negligible energy.

IV. ANTIPARALLEL FILAMENTS

A. Initial conditions

Our previous study of the Biot–Savart model for a vortex filament[1] showed that significant vortex stretching leading to a finite time singularity followed most readily for paired antiparallel vortex tubes. Indeed, any initial conditions we tried would invariably assume this configuration in some region, so we infer that the singularity is globally attracting and, in fact, universal because the dynamical equations for the paired filaments are local. The collapse was sufficiently rapid that the velocity diverged as $(t^*-t)^{-1/2}$ and it was only because of logarithmic terms that the viscosity would eventually halt the collapse. These model results plus the possible association with hairpins in the boundary layer make this the obvious first choice of initial conditions.

Our most extensive runs were made with two discrete symmetries imposed, since intuitively this should not hinder the instability, and a factor of 3 is gained in computation time. More general initial conditions are considered at the end of this section. We therefore took the large component of vorticity to be parallel to z and imposed two reflection planes $x=0$ and $z=0$ with the properties

$$x\to -x,\quad v_x\to -v_x,\quad \omega_x\to +\omega_x,$$
$$v_{y,z}\to +v_{y,z},\quad \omega_{y,z}\to -\omega_{y,z}, \tag{10}$$

and similarly for $z\to -z$. Furthermore, we will take $\omega_z>0$ for $x>0$ so that the mean velocity of the pair is toward negative y. These symmetries in no way inhibit reconnection[41] though of course in the absence of viscosity, since the plane $x=0$ is left invariant by the flow, no new vorticity can be introduced there from elsewhere in the domain. For $|z|$ large, there is a small component of ω_x for $x=0$ that is too

small to show up in the graphics and is dynamically passive, but is responsible for closing the majority of vortex lines.

Somewhat arbitrarily we defined our vortex tubes to have a Gaussian core $\omega(r,z) \sim e^{-r^2/\sigma^2}$ centered on two hyperbolas,

$$x = \pm \left[a \cos(\theta) \sqrt{1 + (z/b)^2} + c/2 \right],$$
$$y = a \sin(\theta) \left[\sqrt{1 + (z/b)^2} - 1 \right]. \tag{11}$$

Our long runs were made with $a = 0.3$, $b = 0.6$, $c = 0.75$, $\sigma = 0.5$, $\theta = 1.35$, and a circulation of $\pi/2$. The vorticity was reduced to zero for large (z) by expanding the core size as a power of $|z|$ so that the two cores eventually overlap and the vorticity cancels.

The general shape adopted in (11) was suggested by the Biot–Savart model. The vortex stretching and mutual induction velocity are both maximal for $z = 0$, where we expect the singularity to appear. Thus the vortex pair advances more rapidly in this plane than for $|z| > 0$. The curvature of each filament is then such that the self-induction velocity pushes them together. The general appearance of the vortex tubes for the standard parameters is shown in Fig. 2.

We filled the tubes with vorticity in two different ways. The first, which we ran longest, consisted in taking ω parallel to $\hat{z}$ everywhere and imposing incompressibility by solving (8) for v and proceeding to integrate. We then observed that certain essential aspects of this flow at later times could be understood qualitatively simply from the Biot–Savart law. To verify these suppositions we reinitialized the Euler code still using (11) but took the vorticity parallel to the hyperbolas. The correspondence with the Biot–Savart law was then semiquantitative at early times and at later times the flow was similar to the previous run, see Sec. IV C. These runs, together with some experimentation with different values of a and b in Eq. (11), have given us a reasonable idea of how general initial conditions evolve. We begin by explaining the initial states of the flow with the Biot–Savart law and then discuss the asymptotics.

Since our initial conditions can be reasonably approximated as vortex tubes, one would expect that the Biot–Savart formula would give an approximate account of the velocity field they induce and hence their initial evolution. Nevertheless, it would be incorrect to assume that the vorticity remains tubelike forever, i.e., adapt a Biot–Savart model, since the cores are known to flatten when they evolve.[27–31]

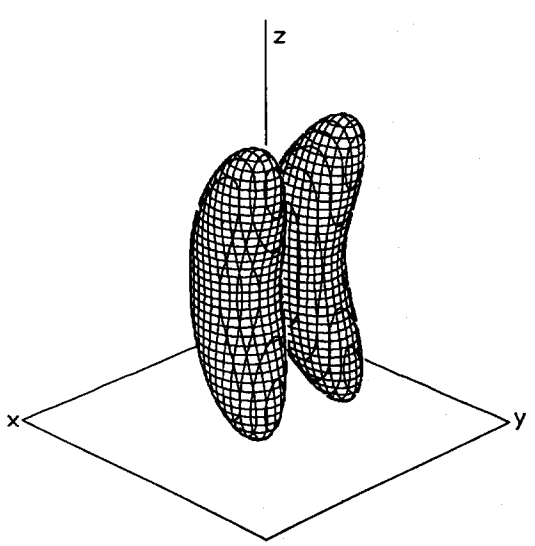

FIG. 2. Isovorticity surfaces bounding the region where $|\omega|$ is greater than 30% of its maximum obtained from Eq. (11) with ω parallel to the hyperbola. The coordinate range is $-2 \le x,y,z \le 2$ and the origin is centered between the tubes. The axes indicate direction only. The vorticity in the left (right) tube is pointed toward positive (negative) z so that the tubes move toward $-y$.

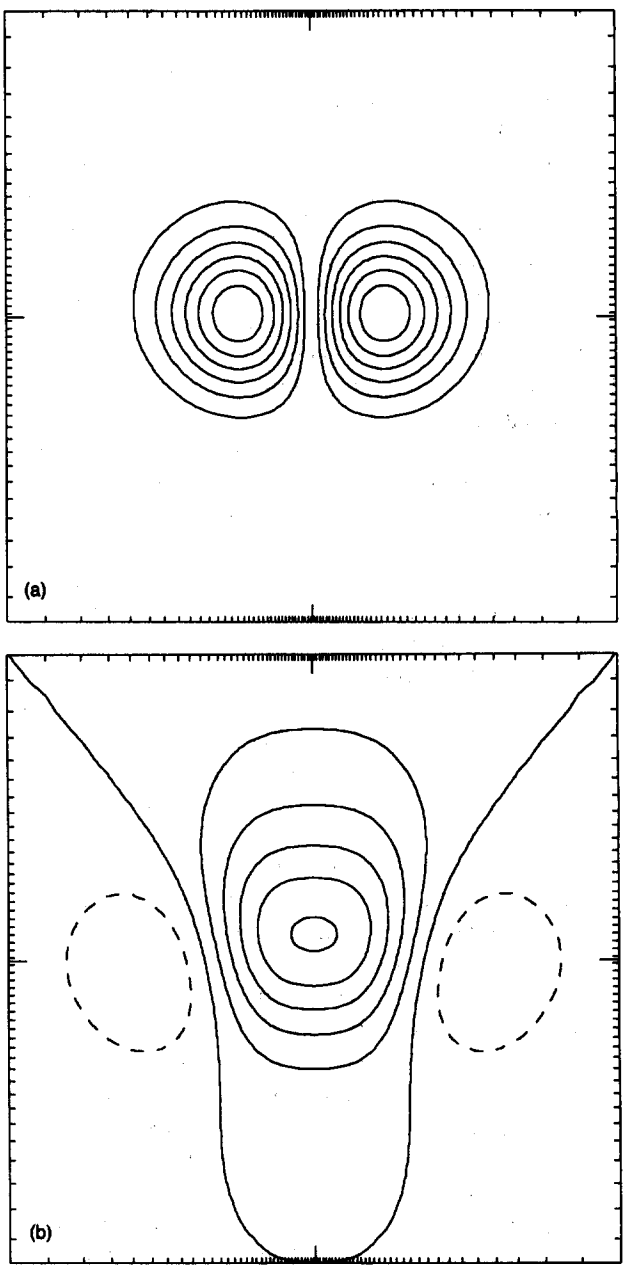

FIG. 3. Contour plots of (a) $|\omega_z|$ and (b) $\partial_z v_z$ in the plane $z = 0$ for the same data as in Fig. 2. The range of coordinates is $-2 \le x,y \le 2$ with x horizontal. At the end of this run, the distance between the vorticity maxima will fit within the thickness of the lines. The small tic marks indicate the computational mesh and the large tic is zero. Dashed lines indicate negative values; and when, and only when, they are present, the lowest solid line is zero. The contour interval is 0.5, (0.1), for (a), (b). Note that the centers of the vortex tubes at $x = \pm c/2, y = 0$, cf. (11), fall in the region $\partial_z v_z > 0$.

We will explain the initial core distortion as essentially a result of the nonuniformity in the vortex stretching that for $z=0$ is just $\partial_z v_z$ by symmetry. The other components of strain are of course present and have been examined but they are dominated by purely two-dimensional effects that for early times will slightly distort the cores but basically produce a stable propagating dipole similar to Fig. 1. The existence of many stable vortex dipole solutions in two dimensions also argues against low pressure in the center of the pair *per se* as the cause of the flattening, since it is predominantly of 2-D origin, too. The axial flow at early times was examined in Ref. 1.

It will be instructive to display explicitly the expression for $\partial_z v_z$ for a single vortex tube lying in the plane $x=0$, symmetric about $z=0$, and given parametrically by $y=\rho\xi(\theta)$, $z=\rho\eta(\theta)$, where ρ is the radius of curvature at $z=0$ and $\theta\epsilon[-1,1]$, viz.,

$$\partial_z v_z(x,y,0) = \frac{-3\Gamma}{4\pi\rho^2}\left(\frac{x}{\rho}\right) \times \int_{-1}^{1} \frac{\eta(d\xi/d\theta)d\theta}{[(x/\rho)^2+(y/\rho-\xi)^2+\eta^2+(\sigma/\rho)^2]^{5/2}}, \tag{12}$$

where Γ is the circulation and σ the core size. Therefore $\partial_z v_z$ as a function of x,y acquires the spatial scale of the curve, ρ, in the z direction, which will be important in what follows. More generally, $\partial_z v_z(x,y,0)$ depends only on ω_x and ω_y and therefore knows about ω_z only implicitly through $\nabla\cdot\omega=0$.

In Figs. 3(a) and 3(b) we show the actual vorticity profile and strain rate in the plane $z=0$ for the standard initial conditions, given below Eq. (11), and vorticity parallel to the tube. Evidently the vorticity will grow most rapidly for $|x|<c/2$, i.e., where $\partial_z v_z>0$.

The maximum will increase only slightly and the vorticity will actually decrease for $|x|\gtrsim c/2$, where $\partial_z v_z$ is negative. Hence there will be a buildup of ω_z in the center without much change in the y extent of the tubes. When ω is parallel to $\hat{z}$ initially, $\partial_z v_z$ is essentially zero everywhere, therefore the effects seen in Fig. 3(b) become prominent only at later times, and the initial flattening of the vortex cores is more owing to the other components of strain.

Figure 3(b) can be understood intuitively by comparing it with $\partial_z v_z$ in Fig. 4(a) computed from the Biot–Savart formula for the two hyperbolas (11). A core size of 0.5 was used but, in principle, this could be adjusted to improve the fit. In Fig. 4(b) we show $\partial_z v_z$ for a single hyperbola, which makes it evident [cf. Eq. (12)] that the sign change in $\partial_z v_z$ and therefore the principal core distortion is due to the stretching action of each tube on itself. A second tube placed at $x\sim -c/2$ in Fig. 4(b) would experience a net amplification. Only this second effect, the interfilament strain, was included in the Biot–Savart model solved in Ref. 1. There it was interpreted as the result of the difference in radial (i.e., normal to the pair of tubes, in the direction $\hat{y}+\epsilon\hat{z}$) velocities, which leads to an increase in arclength of the filament pair and hence vortex stretching.

The self-generated strain of a vortex tube will be reexamined in Sec. V when we simulate a single parabola as a crude model for the tip of a hairpin.

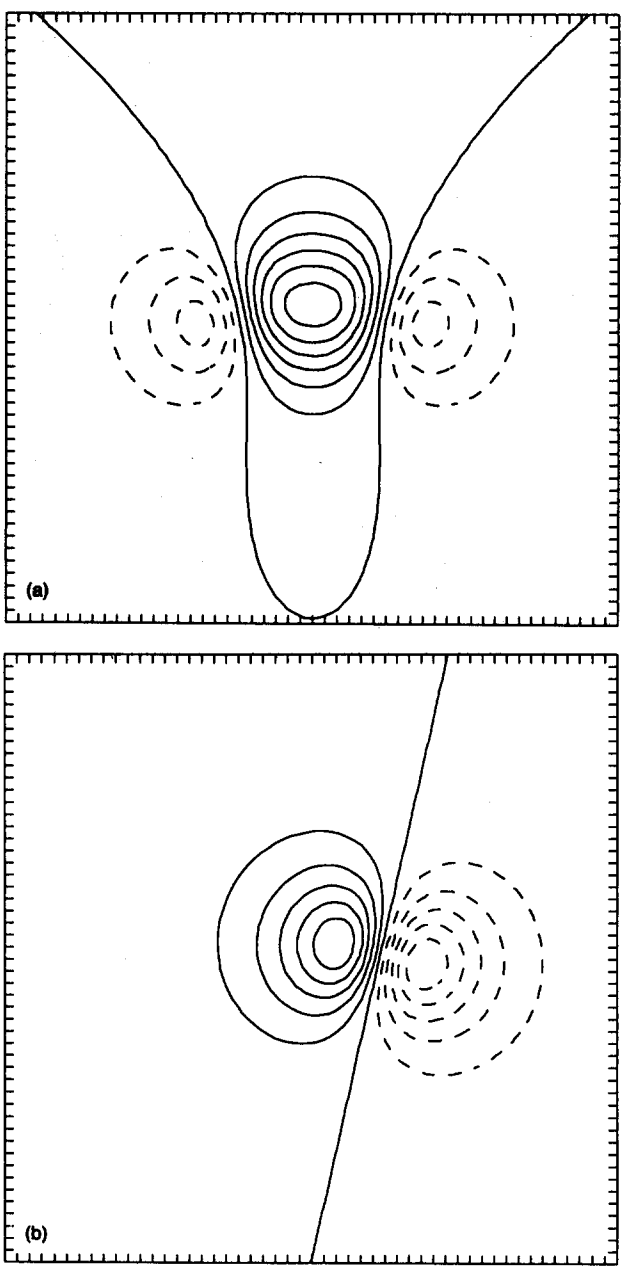

FIG. 4. The stretching $\partial_z v_z$ computed from the Biot–Savart law for (a) two and (b) one hyperbolic vortex filaments (11). The coordinates are the same as in Fig. 3. The diagonal line in (b) is the plane of the hyperbola.

B. Asymptotic evolution

An overview of the run with $\omega\|\hat{z}$ initially is given in Figs. 5–8. The maximum vorticity decreases from its initial value of 3.3 to 2.1 around $T=1.8$. It was always located in the plane $z=0$ except when a parasitic effect occurred around $T\sim 4$ and beyond $T=8.4$, which we discuss more fully below. The vorticity began to grow faster than exponential around $T\sim 6.5$ and became exponential for $T\gtrsim 7.8$. This is perhaps clearer in Fig. 6 where we plot what is approximately the growth rate of maximum vorticity. It saturates slightly after $T=8$, which does not quite correspond to

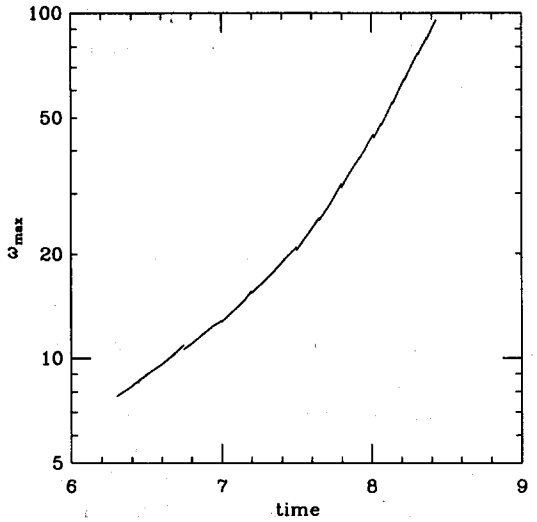

FIG. 5. The evolution of the maximum vorticity on a log scale for the two hyperbolas, and ω initially along z. The initial value of ω_{max} was 3.3 and it decreased to 2.1 before it began to increase monotonically. The small steps occur at each remesh and are due to the smoothing effect of (8).

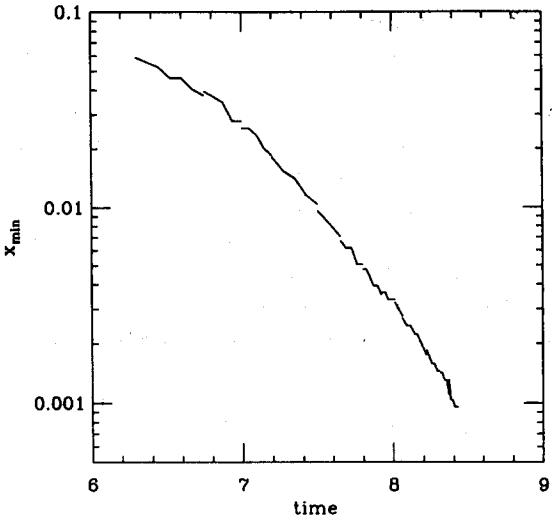

FIG. 7. The distance between the point of maximum vorticity and the symmetry plane $x = 0$ for the data of Fig. 5. The initial value is 0.5 and it decreases monotonically. The irregular appearance of the curve is due to the discrete mesh (no interpolation is done in locating ω_{max}).

Fig. 5 because there is a secular change in shape occurring as will become apparent from the contour plots. The crossover to passive stretching will be explained dynamically below.

It was relatively unambiguous to define a characteristic interior scale in the x direction x_{min} as the distance of the point of maximum vorticity from the symmetry plane $x = 0$ (Fig. 7). Since we sampled the vorticity only at lattice points and did not interpolate, x_{min} has a sampling error of 5%. The initial x_{min} is 0.5, which together with the maximum of the initial velocity field, 1.0, defines a time scale. A second larger "exterior" x scale enters the problem at a later time as will be obvious from the figures.

Length scales in y and z are less well defined. There is definitely structure in the y direction on a scale of several times x_{min} yet the vortex sheets that evolve from the tubes have an extent in y that is ultimately limited by the coordinates to roughly 50 x_{min} for later times ($T \gtrsim 7.2$). There seems to be a single z scale that varies from $O(1)$ to $O(0.1)$ at the end. It is apparent that "sheet" is a very apt term for the vortical structures we find since the y and z dimensions are comparable.

The maximum mean square strain rate, $\mathrm{tr}\, e_{ij}^2, e_{ij} = \frac{1}{2}(\partial_i v_j + \partial_j v_i)$ is shown in Fig. 8. Its location is typically near that of the maximum vorticity in the plane $z = 0$ and its ratio with ω_{max}^2 is 1/2, which is just what one would expect for a velocity varying as $(0,x,0)$. It is also apparent by comparing Figs. 6 and 8 that the maximum strain in the x-y plane is 20 times greater than $\partial_z v_z$ for $T \gtrsim 8$.

Another interesting quantity is the maximum pointwise velocity. It always occurs along the line $x = z = 0$ as one

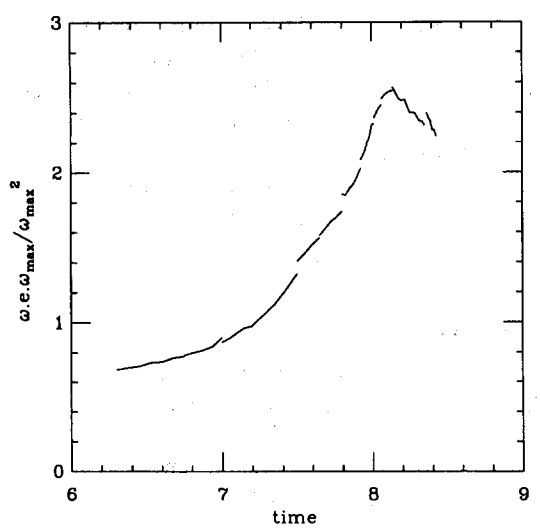

FIG. 6. A qualitative measure of the maximum growth rate of ω^2 for the same data as Fig. 5. The maximum of numerator and denominator is taken separately and occurs at different locations in the $z = 0$ plane. The decrease in the ratio after $T = 8$ is largely due to an increasing separation between where the maxima occur.

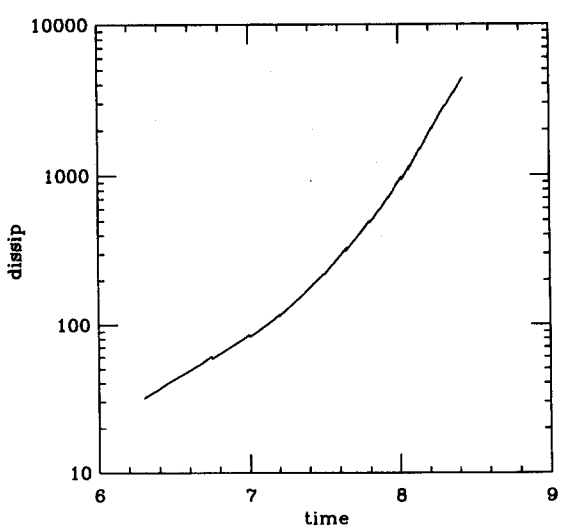

FIG. 8. The mean square strain rate $\mathrm{tr}_{ij}(e_{ij}^2)$, on a log scale for the data in Fig. 5. The initial value is 10.

would expect for a vortex dipole. After we correct for the effects of the cutoff (cf. Sec. III B), it grows from 0.5 to 1.2 at $T = 8$, hence much less rapidly than the vorticity. In view of the Leray bound (2) it is implausible that the stretching is rapid enough to counteract the effects of viscosity.

The energy in the small scales is clearly an important quantity and is crudely measured by the energy contained on the computational mesh. This is constant until we begin to apply the cutoff (cf. Sec. III B) at $T = 7.0$ which removes vorticity around "infinity." This has a minimal effect on the growth rate of $\omega_{\max}$ (cf. the Appendix) (N.B., there is no break in Fig. 5 at $T \sim 7.0$), even though the energy and circulation change substantially.

The cutoff allowed us to decrease the exterior scale of the x (y) mesh [cf. Eq. (3)] by a factor of about 100 (8) from start to finish while the interior scale decreased by a factor of 300 (100). The energy changed from 3.5 to 5×10^{-5}; the total circulation in either sheet decreased from 2.8 to 0.085, while the maximum velocity (not corrected for the remesh), decreased from 1.0 to 0.5. These numbers can be understood crudely by recalling that for paired sheets in two dimensions the energy is of order $\Gamma^2 d/L$, where d is the spacing, L the length, and Γ the total circulation. From $T = 7$ to the end, d decreases by 25, hence the above formula accounts for a factor 3×10^{-4} in the energy change; some of the balance comes from the decrease in the vertical scale. It is surprising but true that the circulation eliminated by the cutoff has a very minimal effect on the growth of $\omega_{\max}$ (see the Appendix).

The evolution in the growth rate of $\omega_{\max}$ apparent from Figs. 5 and 6 can be understood physically from a series of pictures for the vorticity, strain, and circulation at times corresponding to the beginning, end, and middle of Figs. 5–8. We show only the $z = 0$ plane since the resolution requirements are most stringent here. The vortex tubes are less flattened and farther apart for $|z| > 0$. The resolution was also monitored on planes $x = \text{cst}$ and $y = \text{cst}$.

In Figs. 9(a) and 9(b) we show the vorticity and $\partial_z v_z$ at $T = 6.3$ for $x \geqslant 0$. The x axis has been uniformly stretched by a factor of 5 relative to the y axis to make the internal structure of the sheet more apparent. Virtually the entire extent in y of the sheet is visible, which will not be the case at later times since we will retain the same dilatation ratio of 5 to make shape changes more obvious. On dynamical grounds it is apparent that the "tail" of the sheet, $y \gtrsim 0.5$, will not evolve rapidly while the "head" gets pulled into a fine point. The x coordinate of the maximum vorticity will decrease by a further factor of 60 at the final time which corresponds to one-half the spacing between the finest marks in Fig. 9. The stretching is concentrated toward the middle of the sheet and the vorticity that gets amplified is advected forward until it eventually is "shed" and no longer stretched. This "tongue" of shed vorticity will progressively flatten and begin to roll up at later times.

At the next time, 7.2 [Fig. 10(a)], the vortex sheet is more pronounced but there is also more vorticity spread out for $x \gtrsim 2x_{\min}$. The stretching, Fig. 10(b), does not look terribly different from Fig. 9(b) except that the magnitude has doubled. Note that $\partial_z v_z$ varies more gradually with x than

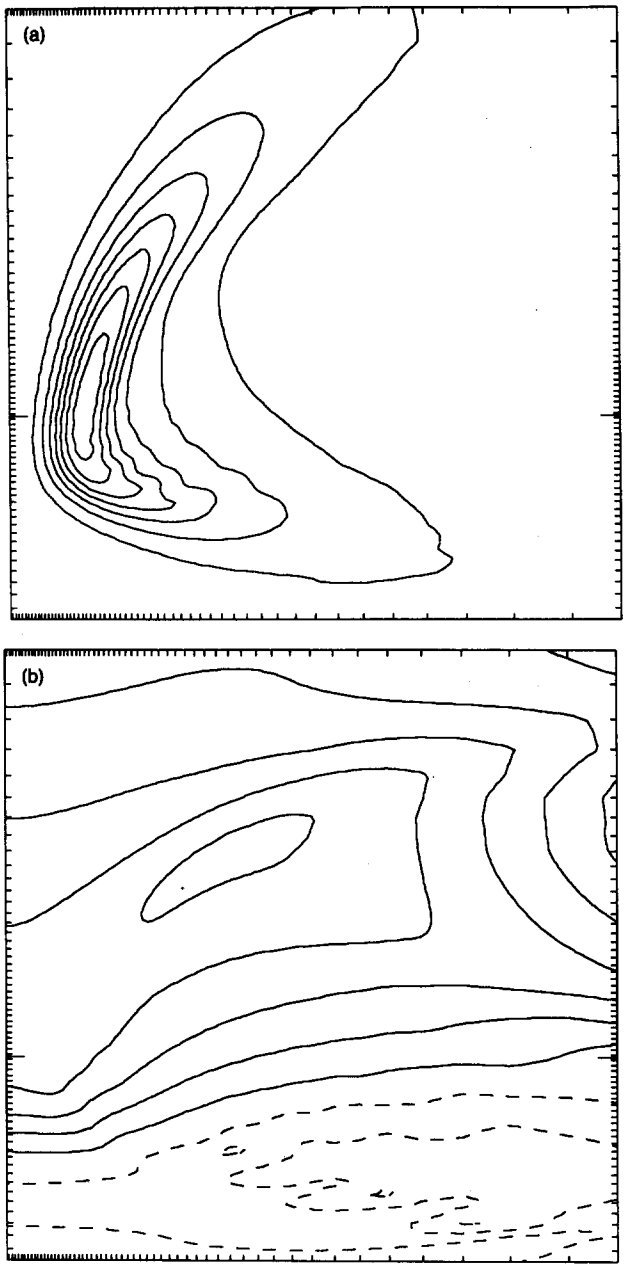

FIG. 9. Contour plots of (a) ω_z, (b) $\partial_z v_z$, in the plane $z = 0$ for the data of Fig. 5 at $T = 6.3$. The coordinate ranges are $0 < x < 0.48$ (the other sheet for $x < 0$ is obtained by reflection), and $-0.8 < y < 1.60$. A uniform dilatation of 5 was applied to x, but otherwise conventions follow Fig. 3. The intrinsic velocity of the two sheets is downward. At the end of the run, the maximum vorticity will lie within half a tic spacing of $x = 0$. The contour interval is 1.0 (a) and 0.2 (b).

does ω_z. It will be important in explaining the crossover to passive stretching for $T \gtrsim 7.8$ to quantify how the circulation is distributed in the plane. This we do in Fig. 10(c) by plotting $\int_0^x \omega_z(x', y, 0)\,dx'$. Vertical parallel contour lines imply a vortex sheet with constant circulation per length. Comparison of Figs. 10(a) and 10(c) shows that about 30% of the circulation is contained in the sheet surrounding the high vorticity region, $x \lesssim 0.035$.

Some impression of the three-dimensional structures is given in Figs. 11(a) and 11(b), again using unequal scales.

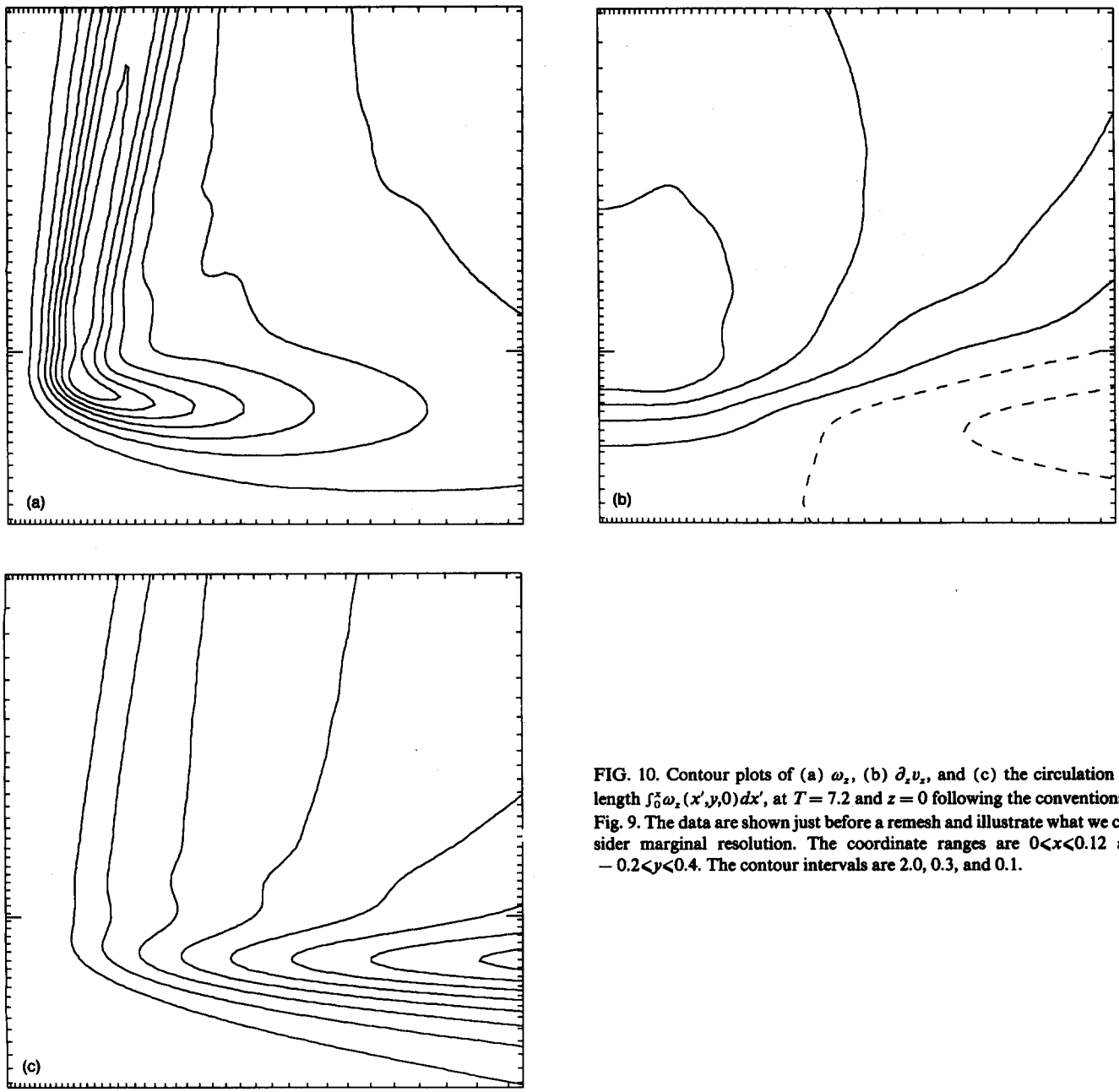

FIG. 10. Contour plots of (a) ω_z, (b) $\partial_z v_z$, and (c) the circulation per length $\int_0^x \omega_z(x',y,0)dx'$, at $T=7.2$ and $z=0$ following the conventions of Fig. 9. The data are shown just before a remesh and illustrate what we consider marginal resolution. The coordinate ranges are $0<x<0.12$ and $-0.2<y<0.4$. The contour intervals are 2.0, 0.3, and 0.1.

The contour level displayed in Fig. 11(a), 40% of the maximum, corresponds exactly to what we identified as the "sheet" in Fig. 10(a). If continued to larger positive y, the sheet in Fig. 10(a) would terminate at $y\sim 1.4$ (and without the cutoff perhaps a factor of 2 further). Note that the extent in z is real and not limited by the graphics. Figure 11(b) shows that the vorticity is very well aligned.

At the final time the trends evident at 7.2 have become more extreme [Figs. 12(a)–12(c)]. The maximum vorticity occurs in a thin sheet that contains less than 15% of the circulation. It is thus plausible that its stretching is passive and generated from the regions of the flow containing most of the circulation. The strain continues to vary more slowly in x than the vorticity, hence virtually the whole of Fig. 12(a) is being amplified except for the "tongue." It is now more apparent that the sheet is stretched rapidly for $y\gtrsim 0$ and then advected around the center of the picture and into the tongue by the preponderance of the circulation. Note that because of the different scalings the "tongue," though thinner proportionally than in Fig. 11(a), is still four times thicker than the sheet.

The "tongue" in three dimensions, Fig. 13(a), gives the vortex sheet more of a shell-like appearance. The vorticity vector [Fig. 13(b)] evidently lies in the plane of the sheet. The forward tilt, which was not evident in Fig. 11(b), is not understood, but is not associated with the cutoff. Since only the intense regions of vorticity are shown it is not clear where the vortex lines end. To determine this, we integrated the equation

$$\frac{\partial \gamma}{\partial t} = \omega$$

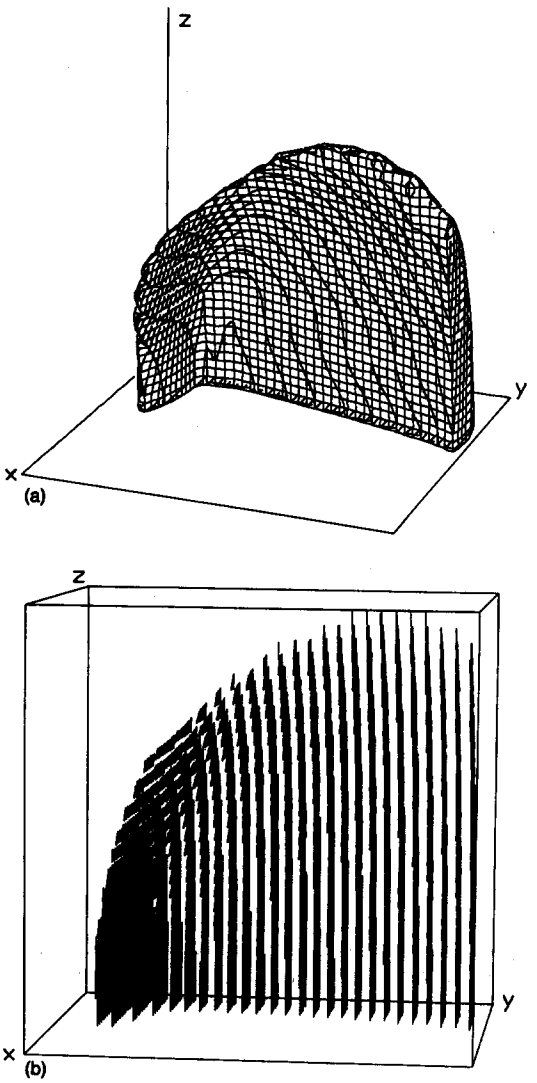

FIG. 11. Isovorticity surfaces (a), and vorticity vectors (b), at $T = 7.2$. Only the region $0<x<0.15$, $-0.15<y<0.90$, and $0<z<0.45$ is shown and the coordinates have been stretched uniformly in the ratio of 1:7:3. The threshold on $|\omega|$ for inclusion in the figure was set to 40% of the maximum in (a) and 30% in (b). The actual grid points are used in (b) while a coarser and uniform mesh was interpolated to draw (a). The axes are drawn at the lower limits of the coordinates.

to find the vortex lines. On the scale of z shown in Figs. 13(a) and 13(b) there was no reconnection between the sheets.

Although the initial tendency for tubes to become sheets was explained as an effect of nonuniform stretching, this seems less plausible at $T = 8.3$ since the sheet is spread over a thin region in comparison with the stretching. In addition, the interior (right-hand) boundary of the sheet ($x \sim 0.003$) is too sharp to be explained this way. In Figs. 14(a) and 14(b) we show $\partial_x v_x$ and $\partial_y v_y$ whose sum must be $-\partial_z v_z$. Uniform gradients in x,y will change the overall scale size but not the relative placement of contour lines. But note that $\partial_x v_x$ itself has an adverse linear gradient and can be crudely fit as

$$\partial_x v_x \sim -5 + \frac{4(x/0.01)^2}{1 + (x/0.01)}, \quad x \lesssim 0.02.$$

Such a flow in one dimension will concentrate density around $x = 0$ and the numbers are semiquantitatively in accord with what is seen. The nonuniformities in $\partial_i v_i$ all act to produce sharp boundaries in the vorticity distribution that we will term vortex jumps.

The integration was continued through several remeshes beyond 8.3 (i.e., $x_{\min}$ decreased another factor of 10 and $\omega_{\max}$ increased by 40%), though the data are not shown in Figs. 5–8. The trends noted at 8.3 all continue but a new numerical instability occurs which effectively terminates the computation. From Fig. 7 it is apparent that the magnitude of the maximum eigenvalues of e_{ij}, which are in the x-y plane, continue to grow exponentially while the z component is constant. Hence any stray vorticity in the x direction, which could be generated when incompressibility is imposed on the initial conditions, when placed in front of the sheets will rapidly amplify in magnitude and compress its support in y. This vorticity has negligible circulation so the stretching is passive but its magnitude can eventually exceed that of ω_z for $z = 0$.

A similar effect was seen for early times in this run $T \sim 3$–4 because the initial conditions made $\partial_z v_z = 0$, while enforcing incompressibility on $\omega = \hat{\omega z}$ causes the vorticity to reconnect in front of the two tubes. This has been seen by other authors, too ("bridging" in Refs. 29, 30, 42), but is of no relevance for singularities since the strain is not generated by the vorticity being strained (see also Sec. V A).

It is plausible but by no means certain that the growth of $\omega_{\max}$ (assumed parallel to $\hat{z}$ and in the $z = 0$ plane) remains exponential for $T \gtrsim 8.4$. Arguing in favor is the tendency of the solution to leave behind (for $+y$) most of its circulation, i.e., the circulation contained in a slab, say, $\Delta y = 10 x_{\min}$ around $\omega_{\max}$, continually decreases. The pronounced break in Fig. 6 is an artifact of how the ratio is defined. For $T \gtrsim 8$, the formation of a thin passively stretched sheet has occurred and it begins to be advected out of the region of greatest stretching. Hence the y position of $\max(\omega \cdot e \cdot \omega)$ vs $\max(|\omega|)$ increases secularly and destroys the utility of the ratio. However, $\max(\partial_z v_z)$ measured directly never becomes larger than 2.6 and does not diverge.

Two more general points of physics should be stressed before considering briefly other related initial conditions. It is quite surprising that the two sheets of antiparallel vorticity we have painstakingly simulated do not exhibit instabilities with a y wave vector $k_y \sim 1/x_{\min}$. Two sheets are similar to a two-dimensional wake (width d), and many calculations have shown that a varicoselike mode, symmetric under $x \to -x$, is unstable for $0 < k_y \lesssim O(2/d)$ and compatible with our symmetry assumptions.[43] There is also abundant time for the instability to develop since the characteristic velocity is always $O(1)$ and from Fig. 6 the spacing between the sheets, $\sim 2x_{\min}$, is $\lesssim 0.02$ for a $\Delta T > 1$. The explanation must lie in the superimposed stretching which is comparable in y [cf. Fig. 14(b)] and z [Fig. 12(b)], but is still only of order $\omega_{\max}/30$. We are not aware of any analytic calculations that precisely address this situation.[44]

Another point worthy of emphasis is the evolution of the vorticity–strain correlations with time or equally well with increase in maximum mean square strain. The eigenvalues of

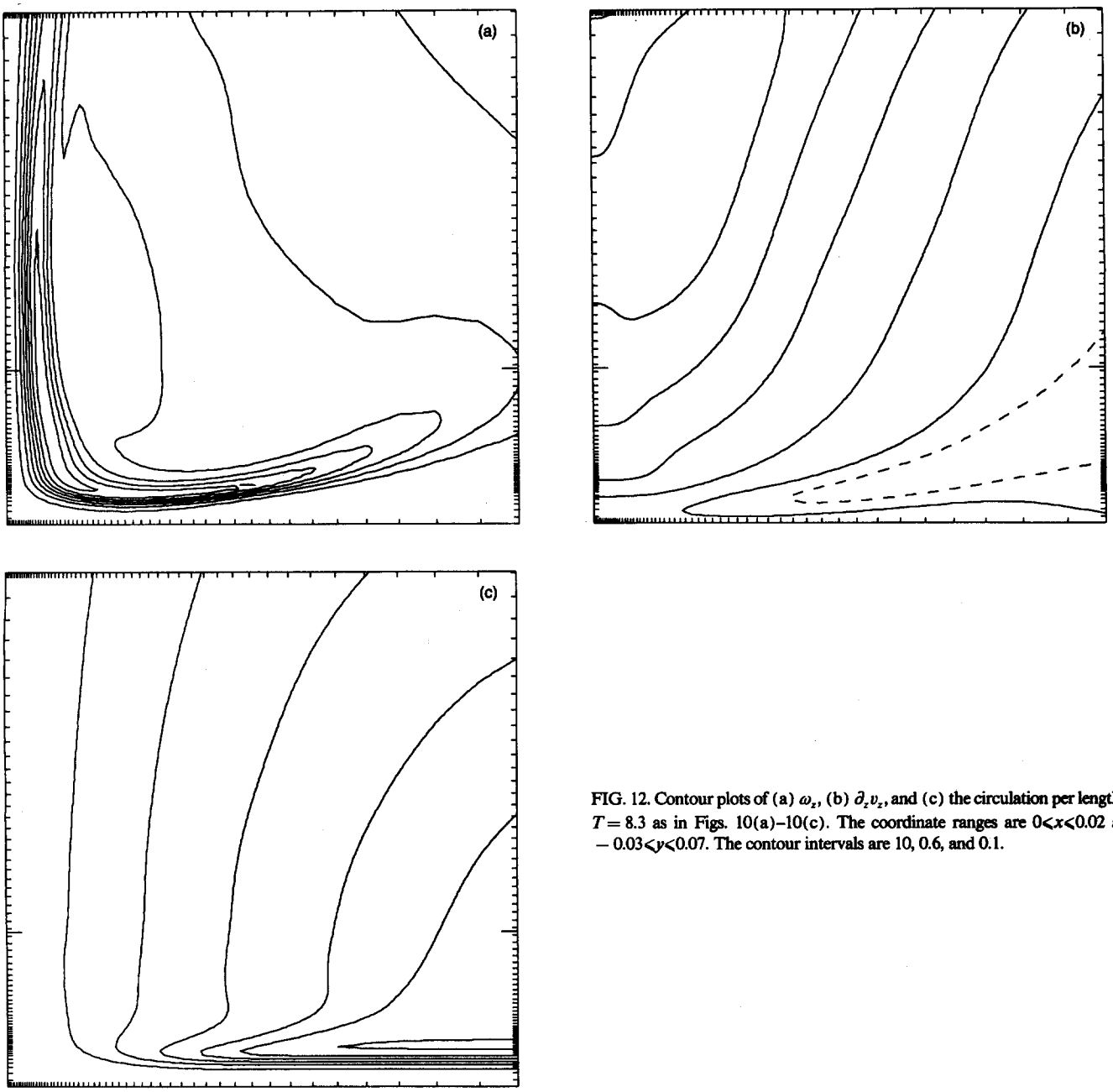

FIG. 12. Contour plots of (a) ω_z, (b) $\partial_z v_z$, and (c) the circulation per length at $T=8.3$ as in Figs. 10(a)–10(c). The coordinate ranges are $0<x<0.02$ and $-0.03<y<0.07$. The contour intervals are 10, 0.6, and 0.1.

the rate-of-strain matrix are proportional to $(1,\epsilon,-1-\epsilon)$ with ϵ a decreasing function of time and the vorticity parallel to the corresponding eigendirection. The flow thus becomes locally two dimensional. A similar tendency has been found in other simulations and will be discussed further in Sec. VI.

C. Related initial conditions

The long run just discussed was initialized with ω parallel to $\hat{z}$ so that initially there was no stretching along $\hat{z}$. The alternative, whose subsequent evolution we now summarize, consisted of taking ω parallel to the tubes [cf. Figs. 3(a) and 3(b)]. The initial growth of ω was more rapid but $\omega\cdot e\cdot\omega/\omega^2$ saturated at a lower value than in Fig. 6. It was never necessary to use the cutoff to control the Poisson inversion (cf. Sec. III B). The vorticity profiles looked more nearly self-similar for a longer time than before, and roughly intermediate between Figs. 9(a) and 10(a). The saturation in $\omega\cdot e\cdot\omega/\omega^2$ was again associated with sweeping the maximum vorticity out of the region between the sheets and into a "tail" as in Fig. 13(a).

Within the basic geometry of two antiparallel tubes three additional configurations were tried. First, we relaxed the symmetry $x\rightarrow -x$ and made the circulations of the two tubes 20% different. The initial flattening was unaffected but the pair rotated in the x-y plane around the tube with larger circulation.

The second experiment consisted of adding a large helicity to the flow by putting an axial velocity along the hyperbola antiparallel but proportional to the local vorticity in magnitude. Its maximum value was $\max(v_z)\sim 0.5$ compared with $\max(v_y)\sim 1.0$. The subsequent evolution was ut-

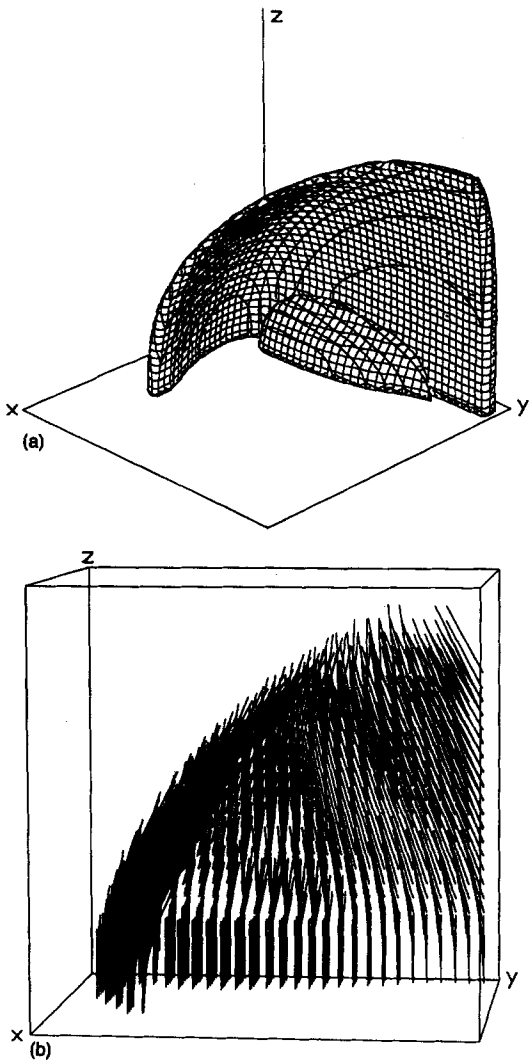

FIG. 13. Isovorticity surfaces (a) and vorticity vectors (b) at $T = 8.3$, as in Figs. 11(a) and 11(b). Only the region $0 \leqslant x \leqslant 0.025$, $-0.03 \leqslant y \leqslant 0.07$, and $0 \leqslant z \leqslant 0.175$ is shown. The thresholds are the same as before.

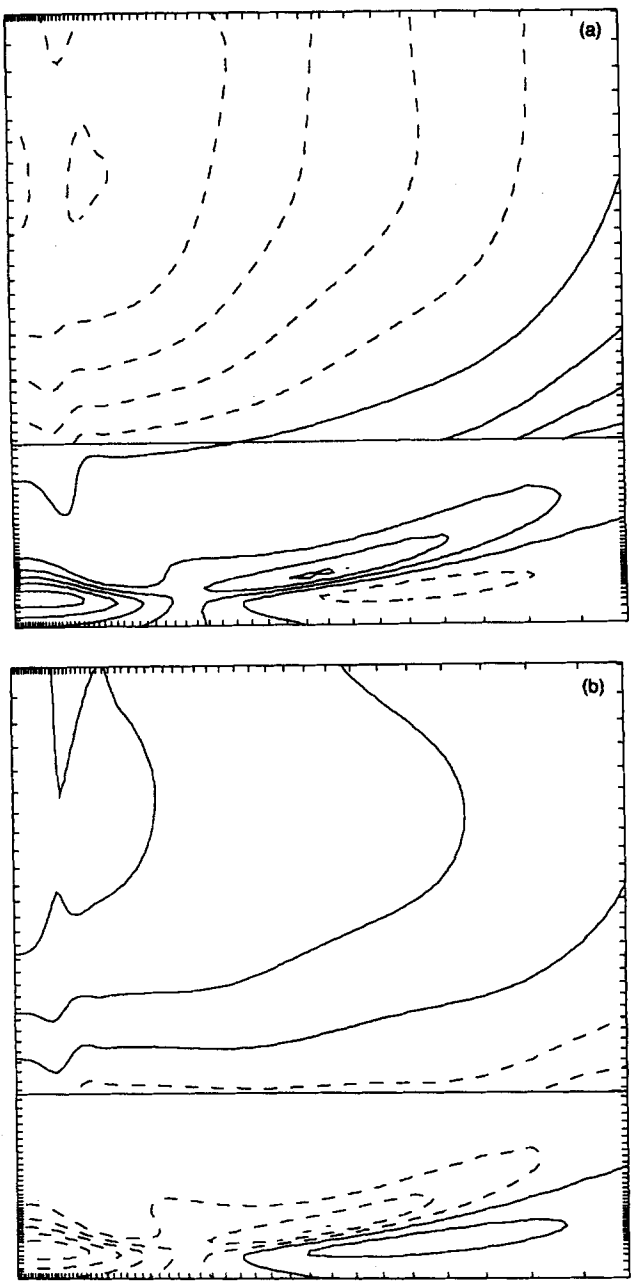

FIG. 14. Contour plots of (a) $\partial_x v_x$ and (b) $\partial_y v_y$, at $T = 8.3$. The coordinate ranges are identical to Fig. 12(a). The contour intervals are 1.0 and 0.9, respectively, in the $y > 0$ portion of each figure, and 6 in the $y < 0$ panel of each figure. The solid horizontal line denotes $y = 0$.

terly different than before and unexpected. The tubes flattened on their outer edges rather than around $x = 0$ and never approached each other. They then proceeded to rotate around the y axis. There was no significant growth in $\omega_{\max}$.

Finally we added viscosity to our long run by restarting the data at $T = 6.75$ with a viscosity so small (3×10^{-5}) as to be negligible, and then waiting for the collapse to reduce the scale size to where viscous effects enter. Once the viscosity induced a small x component of vorticity, the large components of strain amplified it and squeezed it down to a very fine "film" just in front (y more negative) and perpendicular to the principal sheets. Since the x-y strain is growing exponentially, Fig. 8, the vorticity in the "film" grows as $\exp(e^t)$. Separable coordinates were a great handicap and instabilities of the sort which terminated the inviscid run prevented us from integrating far enough for the "film" to acquire significant circulation.

V. OTHER INITIAL CONDITIONS

The paired vortex tubes in the previous section evolved in such a way as to make the vorticity perpendicular to the largest components of the strain and thus avoid a singularity. In this section we devise several initial conditions with higher symmetry and thereby attempt to force vorticity into the plane of greatest stretching. We can conceive of no scenario that would generate these flows "naturally" through successive instabilities, our goal being merely to provoke a singularity. But again, as before, we fail for rather similar reasons. The most intense vorticity is inevitably squeezed into a region where the stretching is passive and where it is rapidly flattened into a sheet. Some experimentation with various parameter values suggests to us that this behavior is typical for these geometries.

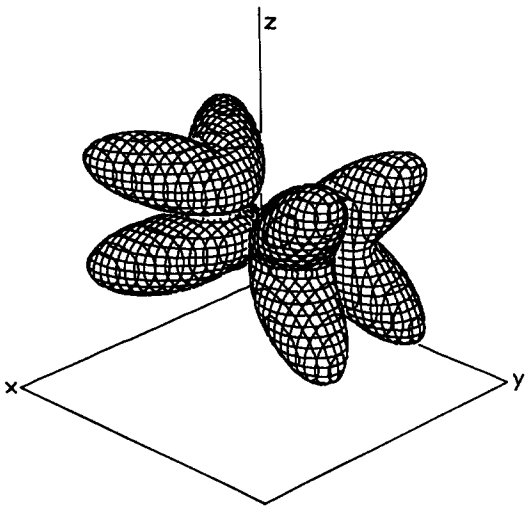

FIG. 15. Isovorticity surfaces for two pairs of hyperbolas initialized according to (11) (with the $y<0$ pair rotated), for $b = 0.3$. The vorticity is directed along the hyperbolas and arranged so as to make the pairs collide in the center.

A. Colliding filament pairs

We were ultimately forced to terminate the integration in Sec. IV because an infinitesimal amount of vorticity in the x direction was amplified and flattened by the exponentially diverging strain rate and caused numerical instabilities. To exploit this effect and make it nonlinear we placed a second pair of hyperbolas perpendicular to the first, i.e., symmetric with respect to the plane $z = 0$ rather than $x = 0$, with vorticity predominantly in the x direction (versus z) and arranged so that the new pair had a positive y velocity. Under the transformation

$$x \to z, \quad y \to -y, \quad z \to -x,$$

the vorticity of the four filaments obeys

$$\omega_x \to -\omega_z, \quad \omega_y \to \omega_y, \quad \omega_z \to \omega_x.$$

We used the same parameters as in (11) to describe each pair but varied b from 0.3 to 1.2. The smaller values of b decreased the radius of curvature at the tip and enhanced the

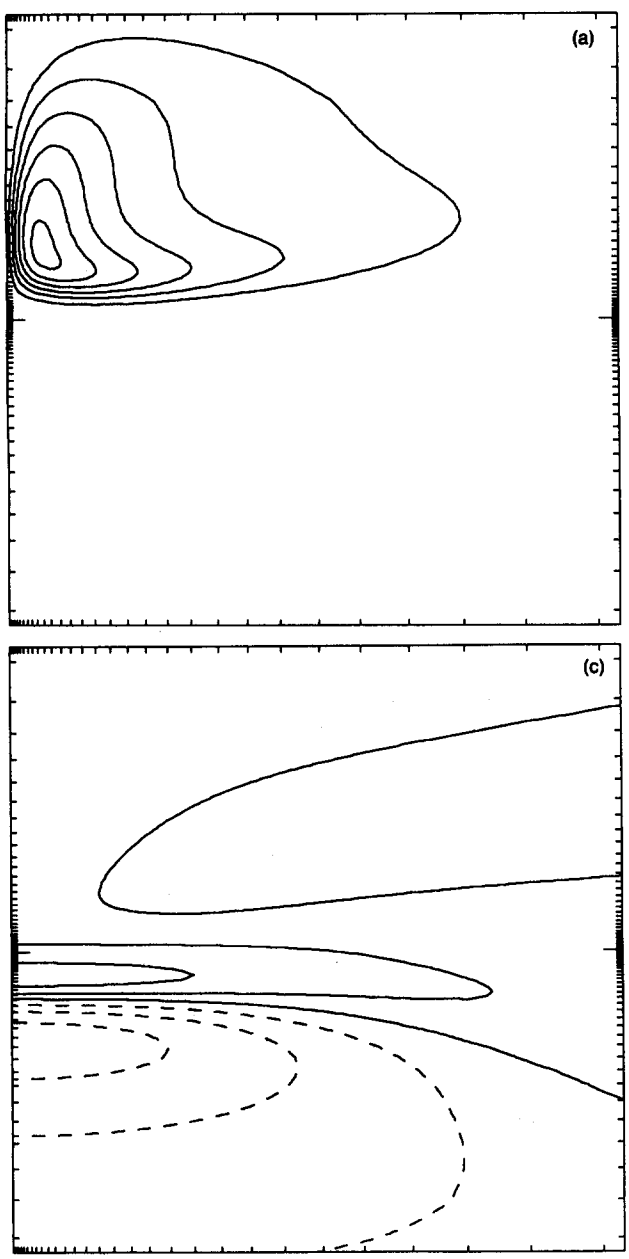

FIG. 16. Contour plots of $|\omega|$ for a plane $z = 0$ (a), $|\omega|$ for a plane $z > 0$ (b), and $\partial_z v_z$ for $z = 0$ (c) all at $T = 2.0$ for the initial conditions in Fig. 15. The coordinate ranges are $0 \leq x \leq 0.75$ and $-1.5 < y < 1.5$. The vorticity in (b) is along $\hat{z}$ for $y > 0$ and along $\hat{x}$ for $y < 0$. The contour interval is 1.0 in all cases.

tendency of each pair to squeeze together by virtue of the self-induction velocity. In this way we attempted, to no avail, to counteract the tendency for the vorticity to be expelled from the region around the origin. Only the data for $b = 0.3$ will be shown.

The initial conditions are displayed in Fig. 15 in three dimensions. Significant interaction between the pairs occurs by $T = 2$ [see Figs. 16(a)–16(c)]. The collision is first felt in the tip whose propagation is impeded by the jet coming from the center of the other pair. As a result, some wraparound begins to be noticeable.

The strain pictures are the most revealing. While the tubes remain roughly circular, the strain field in front of each resembles that of two point vortices. The strong positive stretching in Fig. 16(c) comes from the other pair of tubes with $\omega \| \hat{x}$ and $y \lesssim 0$. Unfortunately it does not project far enough forward in y to overlap the cores of the upper pair of tubes. This scale is roughly determined by the separation in z of the lower pair of tubes for $x = 0$ or by symmetry, the x separation of the upper pair for $z = 0$. The very same compression that was designed to counteract the vortex ejection to follow, thus initially limits the stretching. The more extended but equally intense negative $\partial_z v_z$ also originates from the lower pair and is responsible for squeezing them together. (By symmetry it is identical to $\partial_x v_x$ in the plane $x = 0$ for $y > 0$.)

The final phase of this flow is shown in Figs. 17(a)–17(d). The region of maximum vorticity is rapidly ejected

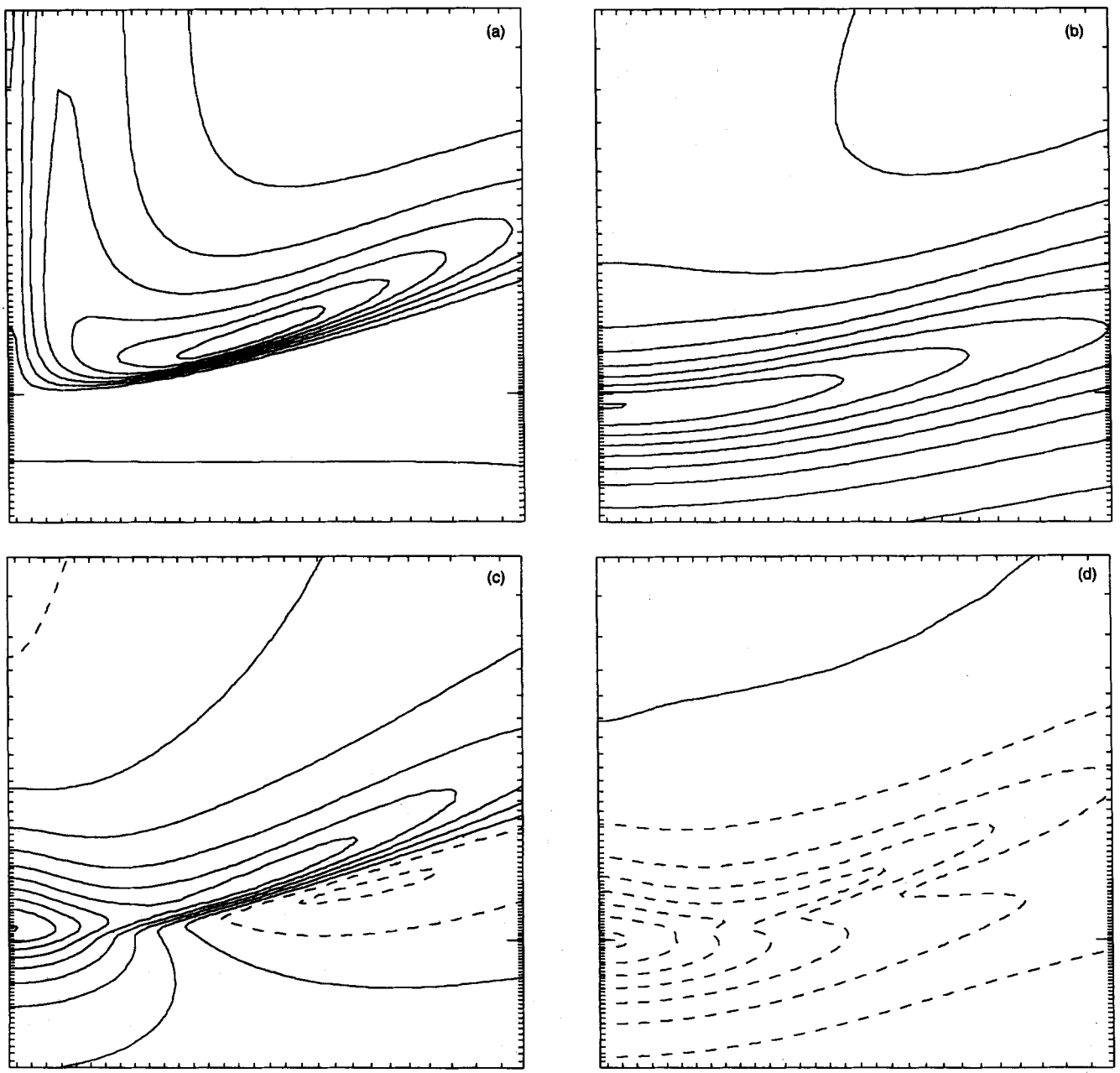

FIG. 17. Contour plots of (a) $|\omega|$, (b) $\partial_z v_z$, (c) $\partial_x v_x$, and (d) $\partial_y v_y$, all for $z = 0$ and $t = 2.75$ for the initial conditions of Fig. 15. The coordinate ranges are $0 < x < 0.2$ and $-0.1 < y < 0.3$. The contour intervals are 2.0, 1.0, 1.0, and 2.0, respectively.

away from the origin. The parallel strain rate $\partial_z v_z$ is positive but growing very slowly at these times. We infer from the overall geometry of the flow that the strain acting for $x>0$ has no reason to diverge in a finite time. It is derived essentially from the dynamics of the lower pair alone since the sheet that is smeared across its upper surface does not carry a lot of circulation. These remarks are rather conjectural since numerical difficulties, more apparent in the $|z|>0$ slices, made it difficult to integrate much beyond 2.75 in a separable coordinate system. Up to that time, however, and with no cutoff, the maximum vorticity grew by a factor of 6, the maximum of $\omega\cdot e\cdot\omega$ by 200, and the enstrophy by only 45%.

The numerical problems originate from the rapid dilatation in x and compression in y visible in Figs. 17(c) and 17(d). The former has its counterpart by symmetry in Fig. 17(b), where $\partial_z v_z$ is now positive for $y<0$ [in contrast to Fig. 16(c)]. For reasons identical to what we saw in Sec. IV [e.g., $\partial_y v_y$, Fig. 17(c), large and negative], the vorticity jumps almost discontinuously from 0 to its maximum value and decays more gradually for y increasing in a manner suggestive of a shocklike mechanism although the vorticity field is divergence free. Away from the symmetry planes, $x=0$ and $z=0$, these strain fields produce two opposing jumps with perpendicular vorticity. More sophisticated adaptive mesh algorithms are required to proceed further.

For larger values of b in Eq. (11) the same sort of vortex ejection was produced but earlier, before the two pairs were as close as here. There is no suggestion of a qualitative change in the evolution of the flow with b that could lead to singularity. We infer that the impossibility of keeping each pair of tubes together is, in part, a consequence of the wraparound effect produced at the origin. This straightens and ultimately reverses (makes negative) an effective curvature of each pair. It was precisely this curvature being large and positive initially (b/a small) that pushed them together in accordance with the Biot–Savart law.

B. Parabolic tubes

If the vorticity in Fig. 15 is projected onto the x-z plane, it would be pointing toward the origin along the $\pm x$ axis and away from the origin on the $\pm z$ axis. Another configuration with four tubes is also conceivable with a different sense of vorticity. Imagine a vortex ring in the x-z plane but stretch the pieces of tube that intersect the coordinate axis out to infinity. The sections of tube nearest the origin on the lines $x=\pm z$ will be advected forward most rapidly and we hoped that the strain field of each pair would stretch the vorticity of the other pair. To minimize the possibilities of reconnection along the coordinates axis, we replaced the deformed circle by four parabolas, reflection symmetric about $x=\pm z$, with the ensemble still retaining a fourfold rotational symmetry. (In retrospect, hyperbolas would have served as well as parabolas.)

The subsequent evolution was a disappointment in that the desired stretching was never seen. It was impossible to get the strain yield to extend far enough from opposite pairs of parabolas to be useful. Instead, the dominant interaction was for each tube to distort itself with only minor amplification of vorticity. Nevertheless, we were amused to find that a similar vortex configuration evolved naturally from the Taylor–Green initial conditions [cf. Figs. 17(c) and 19(b) of Ref. 19]. We comment more on this coincidence in the conclusion.

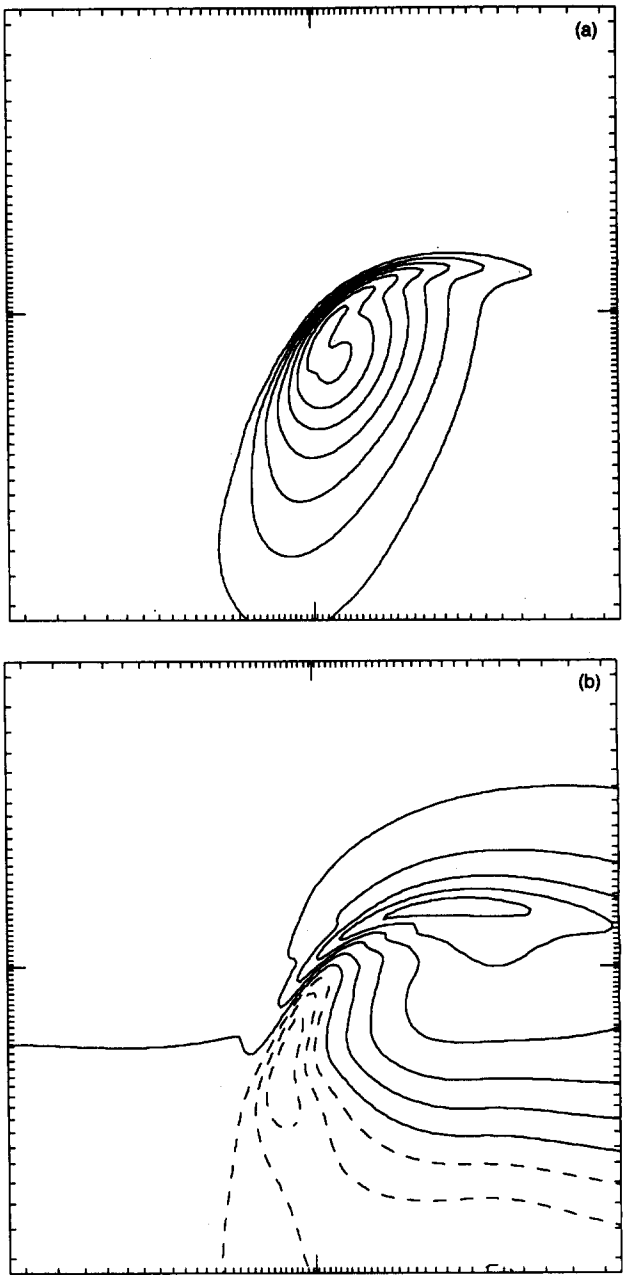

FIG. 18. Contour plots of (a) $|\omega|$ and (b) for $x=0$, $T=3.6$, and for initial conditions consisting of just a single parabola in the x-y plane symmetric under $x\to -x$ (see the text). The coordinate range is $-2<x, y<2$ and the contour interval is 0.3 and 0.1, respectively.

We have pursued a bit further the evolution of a single parabola since it is of some relevance to the tip of a hairpin vortex. When modeled as a vortex filament, the evolution of a parabola is well understood.[45] We comment only on the deformation of the tip, which gives rise to the same sort of vortex "jump" noted in previous sections.

The initial parabola was planar and obeyed $z=0$, $y=1.5x^2$. The core was Gaussian with $\sigma=0.5$ and a circulation of $\pi/2$ as in Sec. IV. The vorticity was parallel to the

parabola. The vorticity normal to the symmetry plane, $x = 0$, of the parabola, which is all the vorticity, as well as the stretching, is shown in Fig. 18 at $T = 3$. Based on the time evolution and examination of the other velocity derivatives, we conclude that the large vorticity gradients result from nonuniform stretching along ω rather than from two-dimensional effects perpendicular to ω.

C. Model of Vieillefosse

The way in which the vorticity produced its own stretching in the previous examples could be understood at least qualitatively from the Biot–Savart equations. A simpler, and in our view less well founded, starting point is what one might term a one-point Lagrangian closure model for the strain and vorticity.[46] The model generates a solution to the Euler equations only if the velocity is proportional to position everywhere, which is unphysical. Nevertheless, the model asymptotically has strain eigenvalues proportional to $(1,\alpha, -1-\alpha)$ with $0<\alpha<1$ and the vorticity along the α direction as was noted in Sec. IV. But the strain and vorticity diverge as $1/(t^*-t)$. We therefore initialized our velocity field with this asymptotic form (ω is a free parameter) and inserted a spatial cutoff of $O(1)$;

$$\mathbf{v} = \frac{1}{(1+\mathbf{r}^2)^2}\begin{pmatrix} \sqrt{9+\omega^2}-1 & -\omega & 0 \\ \omega & -\sqrt{9+\omega^2}-1 & 0 \\ 0 & 0 & 2 \end{pmatrix}\begin{pmatrix} x \\ y \\ z \end{pmatrix}. \tag{13}$$

In Figs. 19(a)–19(c), we show the solution at an intermediate time. The vorticity is along $+z$ in the vicinity of the origin and in the thick parts of the two rings for $z = 0$. Vortex lines circulate around the rings and thus are along $-z$ in the thin parts of the rings where they intersect $z = 0$. They also must close in some diffuse halo around the two rings that is

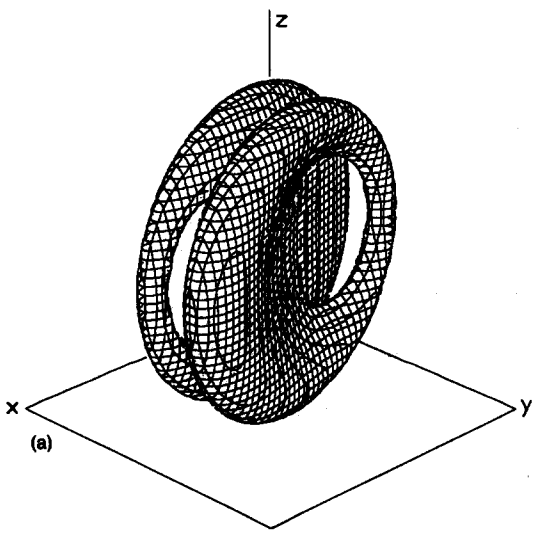

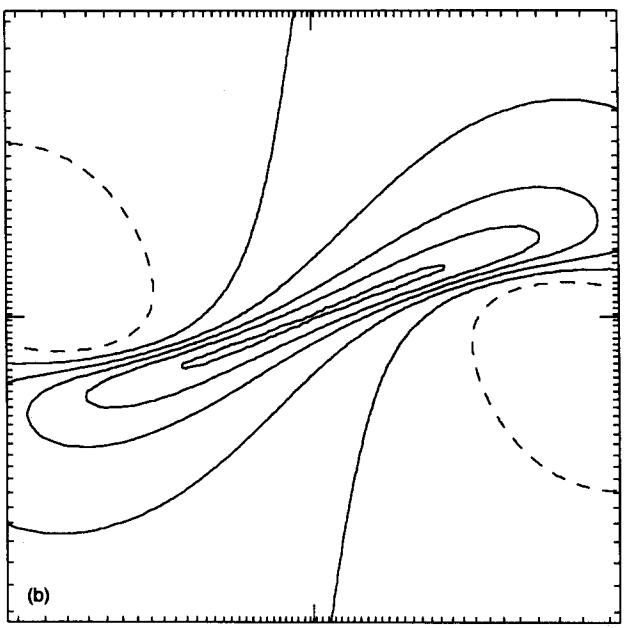

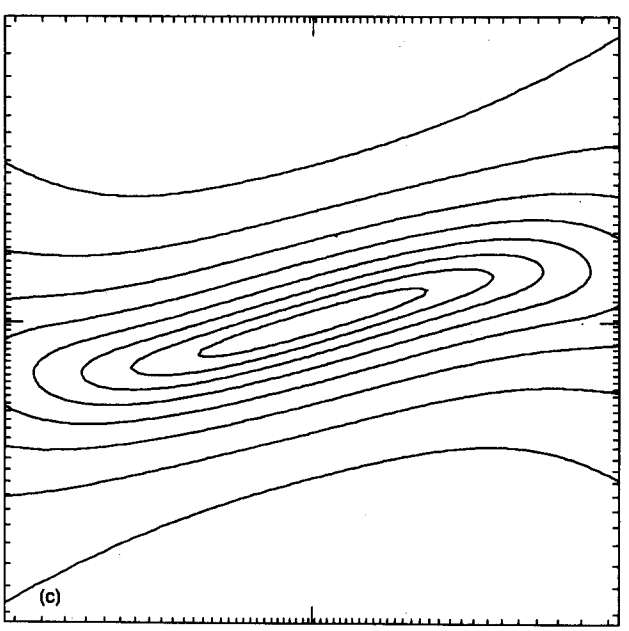

FIG. 19. Isovorticity surfaces (a), ω_z for $z = 0$ (b), and $\partial_z v_z$ for $z = 0$ (c), all at $T = 1.6$ for the initial conditions in Eq. (13). The coordinate range is $-2<x, y<2$ and the contour interval 0.6 and 0.1 in (b) and (c), respectively.

not visible in Fig. 19(a). The sheet surrounding the origin with $\omega \| \hat{z}$ originates from the antisymmetric term in (13). The rings are due to the symmetric terms plus the fact that the velocity decreases to zero at infinity. The shape and distribution of circulation in the tubes suggests that the x and z velocities are positive and increasing at the origin and that $\partial_y v_y$ is negative, giving rise to the flattening.

Figure 19(c) shows that the maximum strain is squarely on top of the vorticity for the first time. Unfortunately the strain rate is monotonically decreasing. This is to be expected since the rings evolve radially outward and simultaneously press together. Both effects tend to minimize their contributions to the velocity gradients at the origin. Other choices for the signs of $\partial_i v_i$ at the origin do not seem any more auspicious for producing a singularity.

VI. CONCLUSIONS

While numerical methods can, under favorable circumstances, make the existence of finite time singularities highly plausible, they are typically much less useful in demonstrating their absence. We therefore first recapitulate what we find and then attempt to make it plausible analytically. We consider whether our failure to find a singularity is a result of limitations of technique or inappropriate initial conditions and review the arguments in favor of singularities.

There are good mathematical reasons for using the growth rate of vorticity to signal a singularity and the exponential growth we found means no finite time singularity. More revealing of the asymptotic dynamics of the flow is $\omega \cdot e \cdot \omega / \omega^2$ in the vicinity of the maximum of vorticity. We find that this quantity saturates to a constant value, precluding growth in ω faster than exponential. This saturation is unambiguous numerically and its interpretation immediate; and it would be interesting to see the same statistic displayed for the Taylor–Green initial conditions. Another statistic that is rather poorly defined for us, but which nevertheless is in accord with the above, is the energy as a function of scale size. For wavenumbers of order $x_{\min}^{-1}(t)$, the energy falls more rapidly than any reasonable power of wavenumber, suggesting that little energy is reaching the small scales. However, we have no direct measure of the energy as a function of time for a fixed $k \ll x_{\min}^{-1}$.

One encouraging aspect of our simulations, as regards their relevance to real flows, is the similarity of the vorticity–strain correlations to those observed in the high dissipation regions in other simulations of developed and quasistationary turbulent flows. More precisely, the vorticity is parallel to the eigenvector of the rate-of-strain matrix corresponding to the intermediate eigenvalue in magnitude which is positive and considerably smaller than the others. (In our case the ratio tends to zero.) This was first seen in Ref. 47, where $\langle \omega \cdot e \cdot e \cdot \omega \rangle$ was no larger than its Gaussian value while $\langle \omega^4 \rangle$ and $\langle e^4 \rangle$ were considerably larger than their respective Gaussian values. The physical meaning of the first correlation is clearer if we write it as $\langle (D\omega/Dt)^2 \rangle$, where D/Dt denotes the Lagrangian derivative. It therefore measures the average vortex stretching, i.e., the rate of strain parallel to vorticity. The same effect was noted more neatly and directly in Ref. 48 for a turbulent shear flow, and in Refs. 48 and 49 for homogeneous isotropic turbulence where the eigenvectors of e_{ij} were computed and correlated with ω at the same point.

Several inferences about the flow can be made directly from this property. Essentially the flow is becoming quasi-two-dimensional with the rate of vortex stretching small compared to the strain rates in the plane perpendicular to the vorticity. As one would expect in two dimensions [think of two point vortices or compare Figs. 12(a) and 12(b) with Figs. 14(a) and 14(b)], the maximum mean square strain and vorticity do not occur in the same place. Also, since the strain is an integral over the vorticity, it is less concentrated in space. The energy cascade becomes less efficient and probably less local when the dominant straining directions are perpendicular to the vorticity, but this does not imply that the nonlinearity is small.[50]

Thus the essential property to explain is why the strain is predominantly perpendicular to vorticity. The vorticity at a point does not generate parallel strain, as is apparent from the integral ($\hat{\rho} \equiv \rho/|\rho|$),

$$(\omega \cdot \nabla) v(r) = -\int \frac{d^3\rho}{4\pi} \frac{\omega(r) \wedge \omega(r+\rho) - 3\hat{\rho} \wedge \omega(r+\rho)\hat{\rho} \cdot \omega(r)}{\rho^3}$$

In the vicinity of $\rho = 0$ and after doing an angular average, the numerator vanishes as ρ^2. Hence with no additional assumptions better estimates should be possible for $\omega \cdot e \cdot \omega / \cdot \omega^2$ than in Ref. 32.

The above equation is purely kinematical. The evolution in time also tends to reduce the parallel components of strain. The essential dynamical ingredient appears to be the property of inviscid hydrodynamics, which makes vortex amplification equivalent to elongation of the parallel line element. Thus stretching reduces the curvature of a vortex line and pushes the perpendicular components of vorticity farther away, thereby reducing the parallel strain. Some additional instability is essential to continuously fold the vortex lines and keep the characteristic length measured parallel to ω the same order as the perpendicular length scales. This instability has to be intrinsic, since asymptotically, extrinsic vorticity has a negligible effect on the collapsed filament pair. Parallel stretching is, however, stabilizing. Hence one can imagine a rather bursty dynamics in which regions stretch, the curvature decreases, till eventually new instabilities occur on the smoothed out vortex field, engendering a new phase of rapid self-stretching. These steps were clearly evident in the simulations of Ref. 1.

If our vortex tubes did not continuously flatten, and the cores remained self-similar, there is little doubt that a finite time singularity would ensue. What happens instead can be rephrased as a decrease in the circulation that is effective in producing strain on the scale of $x_{\min}(t)$. The circulation being most strongly stretched is not responsible for its own stretching. Since the lateral dimensions of the vortex sheets are much greater than their spacing, viewed from the scale of the tip, the contributions of the two sheets tend to cancel.

Is there any core shape, perhaps quite elongated, which evolves without change in shape, but merely changes in scale? We suspect not, but have only a very crude argument

to offer. Energy conservation is not a significant constraint if the characteristic scale of the solution along ω decreases along with the others. Of more interest is the possibility of using circulation integrals in the plane $x = 0$ to show that vortex stretching is accompanied by an increase in a suitably defined integral scale in y. While the vortex pair flow in real space with the symmetry planes we have assumed appears a more tractable problem analytically than that of Taylor and Green, we have not found any general argument other than the symmetry argument of Eq. (12) that necessitates the continual vortex flattening.

By the same token, we are unable to extract a scaling ansatz that leads to a tractable asymptotic expansion for our solutions. The first term is clearly two dimensional as in Ref. 1 but beyond that we have not been able to surmise a choice of scales that would lead to scaled equations that are time independent.

We believe that our simulations have made implausible singular attracting solutions with the assumed discrete symmetries and with well-defined and roughly equal scales in x, y, and z. One could imagine a variety of weaker singularities. For instance, a fixed increment of parallel strain could come from each decade of wavenumber, which could require more care in preserving the large scales than we have exercised. If the singularity is not attracting, additional parameters would have to be adjusted to make the asymptotic solution singular, which we have clearly not done. To pursue this line of reasoning further, we can only mention that we have been unable to construct examples of polynomial systems of ordinary differential equations that are nonsingular for all but exceptional initial conditions. We tend to believe that if a singularity exists it will be attracting but, however, a proof is lacking. We see no hope in excluding singularities for flows other than those we have explicitly examined until we have some analytic understanding of why our flows behave as they do.

The Kolmogorov spectrum for statistically steady-state turbulence implies that the characteristic time necessary to transfer energy from large scales to small ones is finite independent of the range of scales involved. This depends crucially on the spectrum being less steep than k^{-3}, and the conclusion does not carry over to initial value problems for the Euler equations. For any physically reasonable parameters, an exponentially decreasing length, e.g., $x_{\min}$, will hit the viscous scales in a finite time, and one could imagine that the spectrum fills up from high k toward lower k.

The one aspect of turbulence phenomenology that our collapsing solutions do violate is the common assumption that all fields with the same dimensions scale in the same way.[22] This is assumed partially out of ignorance, and also because turbulence is felt to be somehow sufficiently random. This strong scaling assumption clearly leads to finite time singularities since it implies $\omega \cdot e \cdot \omega \sim |\omega|^3$. However, when one is precise, isotropy itself yields no relations among $\langle \omega \cdot e \cdot e \cdot \omega \rangle$ and $\langle \omega^4 \rangle$, $\langle \omega^2 e^2 \rangle$, and $\langle e^4 \rangle$.[51] It would be very interesting to know how the maximum of $\omega \cdot e \cdot \omega / \omega^2$ grows as a function of decreasing viscosity in a statistically steady flow with the large scales prescribed.

The collapsing solutions we have found are of little use in building a coherent structure picture of the energy transfer process. They are simply too inefficient in contrast to the cavitons for the nonlinear Schrödinger equation.[52] We find it encouraging that similar vorticity–strain correlations are seen in simulations of steady-state flows. The mechanism for their generation is apt to be more general than our particular initial conditions, but we hope that the availability of real space data over a large range of scales will facilitate the elucidation of these mechanisms.

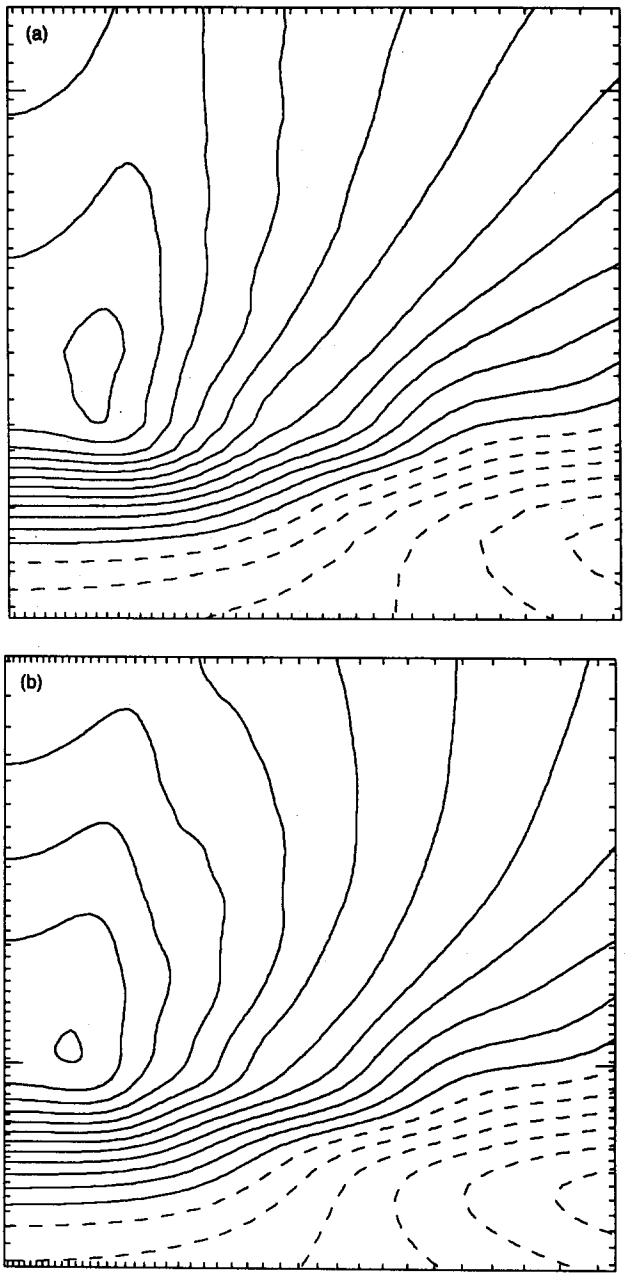

FIG. 20. Contour plots of $\partial_z v_z$ before a remesh (a) and after (b), at $T = 7.0$ and $z = 0$ for the run in Sec. IV. The coordinate limits are $0 < x < 0.12$ and $\Delta y = 0.6$ (the y origin has been shifted). The contour interval is 0.9 in both figures.

ACKNOWLEDGMENTS

We gratefully acknowledge the Cornell Supercomputer Center, the "Service de Physique Théorique" (Saclay), and the "Centre de Calcul Vectoriel pour la Recherche" (Palaiseau) for generous grants of computer time.

Financial support was provided by the National Science

Foundation (NSF) under Grant No. DMR8314625, the U.S. Department of Energy under Grant No. DEAC0283ER13044, and the Guggenheim foundation (E.D.S.).

APPENDIX: NUMERICAL ERRORS

The most suspect step in our algorithm, but also the one that allowed us to attain such small scales, was the remesh. In addition, at later times, it was necessary to discard the vorticity left far behind the singularity which substantially changes integral properties of the flow but not the growth rate of ω_{max} (cf. Sec. III B). These changes were by far the largest $T = 7.0$ when we applied the cutoff for the first time. This was intentional since it is easier to recognize an error if it happens all at once rather than being spread over several remeshes. We therefore dwell on this time.

The energy, enstrophy, maximum velocity, and circulation change by factors of 30, 3.8, 1.5, and 2.68, respectively, but the maximum of $\omega \cdot e \cdot \omega$ changes by only 4.7%. This is partially accounted for by the 0.8% decrease in ω_{max} caused by the smoothing effect of Eq. (8), (which decreases e by a comparable amount).

In the region around the singularity comparable to Fig. 10(a), we show in Figs. 20(a) and 20(b) $\partial_z v_z$ before and after the remesh. The differences between the vorticity contour plots are much smaller since Eq. (8) acts as a diffusion, i.e., is local whereas $\partial_z v_z$ is an integral over all the vorticity. Thus Figs. 20(a) and 20(b) represent the change in $\omega \cdot e \cdot \omega$. We believe this is the most sensitive predictor as to how errors in the initial conditions affect the subsequent development of the singular region. At this time, the cutoff had its greatest effect at $y = -\infty$. It is the nature of our algorithm that if the separation between the sheets is sufficiently small, "infinity" is $O(1)$.

Our final check was simply to remesh the data at 7.0 without a cutoff and evolve it to compare with what was found previously at 7.2, at which time a new remesh was necessary to maintain resolution. The maximum of $\omega \cdot e \cdot \omega$ was reduced 1.7% by the cutoff above [hence the remaining 3% change comes from the smoothing effects of (8) as surmised in the previous paragraph]. At $T = 7.2$ the maxima of ω and $\omega \cdot e \cdot \omega$ were 15.6 vs 15.8 and 237 vs 246. Their values at $T = 7.0$ were 12.8 and 140, respectively. Vorticity contour plots at 7.2 were indistinguishable on the scale of Fig. 10(a) from those previously obtained.

A more typical remesh with cutoff (and in this case also a "smoothing") is at $T = 8.3$ and we show $\partial_z v_z$ before in Fig. 21 and after in Fig. 12(b). The correspondence is better than at $T = 7.0$ and the energy only decreases by 40%.

The resolution is conveniently assessed by displaying all the data on the ξ mesh in Fig. 22. The resolution is marginal in the "tongues" that are thrown off the front of the two sheets but this does not affect the central region where the maximum vorticity is. A better choice of the ξ function mapping in (4) would improve this situation.

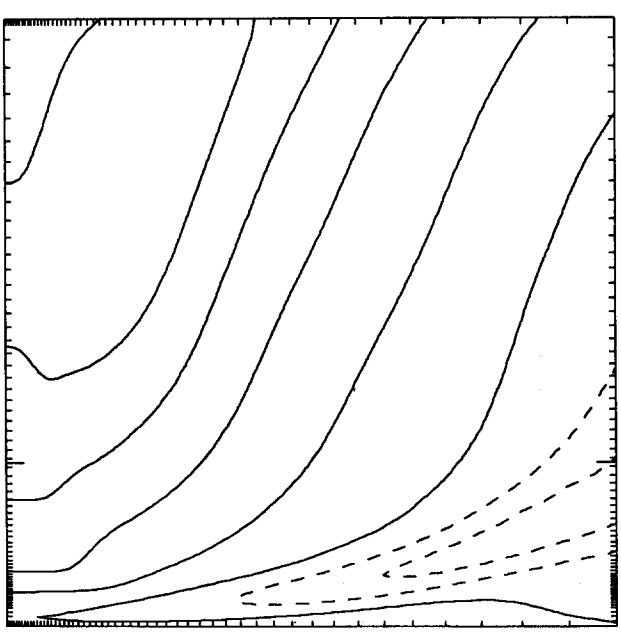

FIG. 21. Contour plot of $\partial_z v_z$ at $T = 8.3$ and $z = 0$ before the remesh. It should be compared with Fig. 12(b), which is after the remesh and is in identical units.

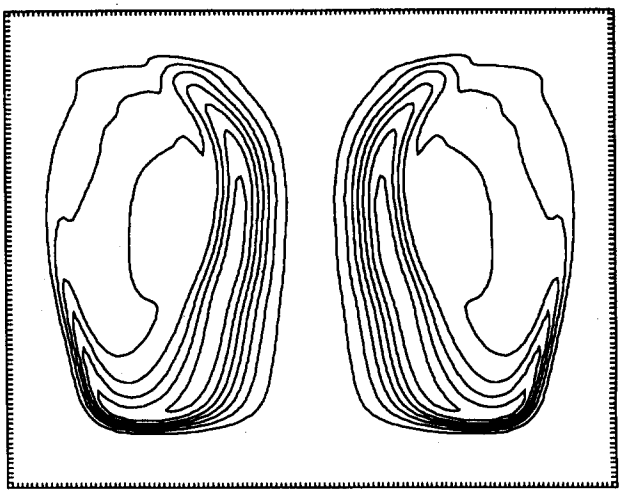

FIG. 22. Contour plots of $|\omega|$ at $T = 8.3$ and $z = 0$ on the numerical, ξ, mesh showing how the vorticity is distributed. The boundaries correspond to $\pm\infty$.

[1] E. D. Siggia and A. Pumir, Phys. Rev. Lett. **55**, 1749 (1985); A. Pumir and E. D. Siggia, Phys. Fluids **30**, 1606 (1987).
[2] A. Pumir and E. D. Siggia, Physica D **37**, 539 (1989).
[3] S. Kline, W. Reynolds, F. Schraub, and P. Runstadler, J. Fluid Mech. **30**, 741 (1967).
[4] H. Kim, S. Kline, and W. Reynolds, J. Fluid Mech. **50**, 133 (1971).
[5] J. Hintz, *Turbulence* (McGraw-Hill, New York, 1959).
[6] L. Landau and E. Lifshitz, *Fluid Mechanics* (Pergamon, London, 1959).
[7] G. Barenblatt, *Similarity, Self-Similarity, and Intermediate Asymptotics* (Consultants Bureau, New York, 1979).
[8] W. Willmarth and T. Bogar, Phys. Fluids **20**, S9 (1977).
[9] F. Frenkiel and P. Klebanoff, Boundary Layer Meteorol. **8**, 173 (1975).
[10] W. Willmarth and S. Lu, J. Fluid Mech. **55**, 65 (1972).
[11] S. Lu and W. Willmarth, J. Fluid Mech. **60**, 481 (1973).
[12] R. Adrian and P. Moin, J. Fluid Mech. **190**, 531 (1988).
[13] M. Head and P. Bandyopadhyay, J. Fluid Mech. **107**, 297 (1981).
[14] P. Moin and J. Kim, J. Fluid Mech. **155**, 441 (1985); J. Fluid Mech. **162**, 339 (1986).
[15] J. Kim, Phys. Fluids **28**, 52 (1985).
[16] B. Bayly, S. Orszag, and T. Herbert, Annu. Rev. Fluid Mech. **20**, 359 (1988).
[17] G. Batchelor and A. Townsend, Proc. R. Soc. A **199**, 238 (1949).
[18] A. Kuo and S. Corrsin, J. Fluid Mech. **50**, 285 (1971).
[19] M. Brachet, D. Meiron, B. Nickel, S. Orszag, and U. Frisch, J. Fluid Mech. **130**, 411 (1983).

[20] A. J. Chorin, Commun. Math. Phys. **83**, 517 (1982).
[21] C. Anderson and C. Greengard (private communication).
[22] M. Nelkin, J. Stat. Phys. **54**, 1 (1989). (It is not evident *a priori* that the initial value problem for the Euler equations has anything to do with isotropic turbulence as it is generally considered.)
[23] M. Berger and R. Kohn, Commun. Pure Appl. Math. **41**, 841 (1988).
[24] B. LeMesurier, G. Papanicolaou, C. Sulem, and P. Sulen, Physics D **31**, 78 (1988).
[25] M. Berger and J. Oliger, J. Comput. Phys. **53**, 484 (1984).
[26] We justify this factor in Sec. III.
[27] A. Pumir and R. Kerr, Phys. Rev. Lett. **58**, 1636 (1987).
[28] D. Meiron, M. Shelley, W. Ashurst, and S. Orszag, "Mathematical Aspects of Vortex Dynamics," in *SIAM Proceedings*, edited by R. Caflish (1989).
[29] N. Zabusky and M. Melander, Physics D **37**, 555 (1989).
[30] R. Kerr and F. Hussain, Physics D **37**, 474 (1989).
[31] K. Sharif, A. Leonard, N. Zabusky, and J. Ferziger, Fluid Dyn. Res. **3**, 337 (1988).
[32] T. Beale, T. Kato, and A. Majda, Commun. Math. Phys. **94**, 61 (1984).
[33] J. Leray, Acta Math. **63**, 193 (1934).
[34] J. Serrin, Arch. Rat. Mech. Analy. **9**, 187 (1962).
[35] L. Caffarelli, R. Kohn, and L. Nirenberg, Commun. Pure Appl. Math. **35**, 771 (1982).
[36] P. Constantin, Commun. Math. Phys. **104**, 311 (1986).
[37] The most effective simulation of this type is Ref. 30. The graphics unfortunately do not permit one to assess the resolution as a function of time.
[38] A more elegant way of achieving comparable accuracy and conservation properties is described in J. Kim and P. Moin, J. Comput. Phys. **59**, 308 (1985).
[39] E. Siggia and A. Pumir, J. Comput. Phys. **72**, 498 (1987).
[40] G. Batchelor, *An Introduction to Fluid Dynamics* (Cambridge U.P., New York, 1974), p. 535.
[41] W. T. Ashurst and D. Meiron, Phys. Rev. Lett. **58**, 1632 (1987).
[42] S. Kida, *Proceedings of IUTAM Symposium on Fundamental Aspects of Vortex Motion*, Tokyo, 1987; Fluid Dyn. Res. **3**, 257 (1988).
[43] P. Drazin and W. Reid, *Hydrodynamic Stability* (Cambridge U.P., New York, 1982).
[44] J. Neu, J. Fluid Mech. **143**, 253 (1984); D. Dritschel, J. Fluid Mech. **206**, 193 (1989).
[45] P. Moin, A. Leonard, and J. Kim, Phys. Fluids **29**, 955 (1986).
[46] P. Vieillefosse, J. Phys. (Paris) **43**, 837 (1982).
[47] E. D. Siggia, J. Fluid Mech. **107**, 357 (1982).
[48] W. Ashurst, A. Kerstein, R. Kerr, and C. Gibson, Phys. Fluids **30**, 2343 (1987).
[49] R. Kerr, Phys. Rev. Lett. **59**, 783 (1987).
[50] R. H. Kraichnan and R. Panda, Phys. Fluids **31**, 2395 (1988).
[51] E. D. Siggia, Phys. Fluids **24**, 1934 (1981).
[52] A. Newell, D. Rand, and D. Russel, Phys. Lett. A **132**, 112 (1988).